JGR Oceans

RESEARCH ARTICLE
10.1029/2021JC017257

Spatial and Temporal Variability of Diapycnal Mixing in the Indian Ocean

K. Katsumata[1], L. D. Talley[2], T. A. Capuano[3], and C. B. Whalen[4]

[1]Research Institute for Global Change, JAMSTEC, Yokosuka, Japan, [2]Scripps Institution of Oceanography, UCSD, San Diego, CA, USA, [3]Departmento de Oceanografia de Universidade Federal de Pernambuco (UFPE), Laboratorio de Oceanografia Fisica, Estuarina, e Costeira (LOFEC), Recife, Brazil, [4]Applied Physics Laboratory, Seattle, WA, USA

Key Points:

- In meridional section, turbulence variability is larger spatially than temporally; thus basin-scale turbulence "geography" is repeatable
- Correlations of diapycnal diffusivity with bottom topography roughness & surface winds were used to map the turbulence in the Indian Ocean
- Additional mixing such as unobserved events, near-bottom turbulence, & equatorial mixing is necessary to close the buoyancy budget

Supporting Information:

Supporting Information may be found in the online version of this article.

Correspondence to:

K. Katsumata,
k.katsumata@jamstec.go.jp

Citation:

Katsumata, K., Talley, L. D., Capuano, T. A., & Whalen, C. B. (2021). Spatial and temporal variability of diapycnal mixing in the Indian Ocean. *Journal of Geophysical Research: Oceans*, *126*, e2021JC017257. https://doi.org/10.1029/2021JC017257

Received 5 FEB 2021
Accepted 17 JUN 2021

Abstract The rate of turbulent kinetic energy dissipation and diapycnal diffusivity are estimated along 10 hydrographic sections across the Indian Ocean from a depth of 500 m to the seabed. Six sections were occupied twice. On the meridional section, which is nominally along 95°E, spatial patterns were observed to persist throughout the three occupations. Since the variability in diffusivity exceeds the variability in the vertical gradients of temperature and salinity, we conclude that the diffusive diapycnal fluxes vary mostly with diffusivity. In high latitudes, diapycnal diffusions of both temperature and salinity contribute almost equally to density diffusion, particularly across isopycnals just above the salinity maximum, while mainly temperature contributes in other latitudes. The known zonal difference in turbulence is reproduced. Diffusivity from the seabed to 4,000 m above the seabed has an exponential profile with a mode value of 4×10^{-4} m^2s^{-1} at 1,000 m above the seabed and is positively correlated with topographic roughness as reported previously. It is found that the diffusivity also correlates with wind power injected through the surface at near-inertial frequencies 10–80 days before the observations. These correlations were used to interpolate the observation-based turbulence quantities to the entire Indian Ocean. Although the dissipation averaged along selected neutral-density surfaces is less than the dissipation needed to explain the meridional overturning circulation evaluated across 32°S latitude, this may be explained by effects not captured by the ship-based observations and parameterization. These effects likely include unobserved high-mixing events, near bottom processes (e.g., hydraulic jumps), and deep equatorial jets.

Plain Language Summary The ocean transports heat and freshwater in north-south directions by the meridional overturning circulation, by which an inflow at some density returns at another density. The circulation requires mixing to convert the inflow into the outflow. We estimated this mixing using data collected from 10 sections that criss-crossed the Indian Ocean. The mixing varies spatiotemporally, but in a section along 95°E, persistent spatial patterns were found during three occupations in 1995, 2007, and 2016. The fluxes across the density surfaces associated with the mixing of temperature and salinity vary primarily with the strength of turbulence; the impacts of the fluxes associated with temperature and salinity on the density of the seawater are comparable at high latitudes. The strength of turbulence depends on the roughness of bottom topography. The smooth bottom and greater depth of the eastern basins result in weaker mixing than the western basins. Turbulence also depends on surface winds. We used these relationships to estimate mixing in the entire Indian Ocean. Mixing was found insufficient to account for the mixing needed to explain the observed meridional overturning circulation. This deficit might be explained by consideration of unobserved high-mixing events, enhanced mixing near the bottom, and mixing by deep equatorial jets.

1. Introduction

Two major deep water masses in the world oceans, Antarctic Bottom Water and North Atlantic Deep Water, return to the surface both adiabatically (Toggweiler & Samuels, 1998; Webb & Suginohara, 2001) and diabatically (Munk & Wunsch, 1998). In the Indian and Pacific Oceans, the deep water upwells to the surface mostly diabatically across density surfaces (Talley, 2013). Although the area of the Indian Ocean is less than half that of the Pacific (north of 60°S), the upwelling, as quantified by the peaks of the meridional overturning streamfunction, are comparable in the two basins. The upwelling in both basins is on the order of 10 Sv (1 Sv = $10^6 m^3 s^{-1}$) (e.g., Hernández-Guerra & Talley, 2016). This is likely due to the relative abundance of

rough topography in the Indian Ocean compared with the Pacific Ocean (Goff & Arbic, 2010). Jayasankar et al. (2019) reported sensitivity of the Indian Ocean meridional overturning circulation simulated in reanalysis products to the model configurations, particularly the bottom topography. The western basins of the Indian Ocean are covered by such topographic features as the Southwest and Central Indian Ridges and Mascarene Plateau. Turbulence is known to be stronger in the western basins than in the eastern basins (Drijfhout & Naveira Garabato, 2008; Kunze, 2017). We quantified this relationship between roughness and diapycnal mixing and mapped the spatial distribution of mixing in the Indian Ocean using hydrographic data obtained with Conductivity, Temperature, and Depth profiler (CTD), horizontal velocities with Lowered Acoustic Doppler Current Profiler (LADCP), and the Gregg-Henyey-Polzin parameterization (Polzin et al., 2014). Our data sets cover most of the sections used by Huussen et al. (2012), the Indian Ocean sections used by Kunze (2017) and data from recent cruises up to 2020. Seven sections were occupied two or three times, and in those cases we averaged the estimated quantities to reduce statistical uncertainties. For all sections, we used both shear from LADCP data and strain from CTD data. The first purpose of this paper is to describe the mixing "geography" in the Indian Ocean using these updated data. We study the 95°E section in detail, which have been occupied three times in 1995, 2007, and 2016. Not only the spatial variations of the diffusivity, but also the spatial variations of the temperature and salinity fluxes contributes to the variations of upwelling. We found the contributions to the variability of upwelling from temperature and salinity to be comparable, particularly at high latitudes.

On a global scale, upwelling must be balanced by the production of deep and bottom water masses at high latitudes in the North Atlantic and shelves around Antarctica. The production of this deep and bottom water requires a vertical diffusivity of $\sim 10^{-4} m^2 s^{-1}$ to account for the required mixing of a water column with the known density structure. The difference between this vertical diffusivity and the diffusivity inferred from in situ measurements of turbulent microstructure ($\sim 10^{-5} m^2 s^{-1}$ in the open ocean far from boundaries) has recently been explained by the adiabatic outcropping of Circumpolar Deep Water in the Southern Ocean (Marshall & Speer, 2012; Webb & Suginohara, 2001) and a careful compilation of in situ measurements that have included the near-boundary enhanced mixing (Waterhouse et al., 2014). Under steady-state conditions, this balance between the deep and bottom water inflow and diapycnal mixing must be closed in each of the Atlantic, Pacific, and Indian Oceans. In the Indian Ocean, Huussen et al. (2012) have estimated the diapycnal mixing north of 32°S from ship-based hydrographic observations and have found that the mixing is insufficient to sustain the meridional overturning circulation north of 32°S. They have pointed out several reasons for the discrepancy: Unobserved mixing "hotspots" and unparameterized boundary mixing, including breaking topographic waves with vertical scales less than the critical vertical scale for parameterization, and hydraulic jumps in locations such as fracture zones. The second purpose of this paper is to update the estimate of Huussen et al. (2012) by using more recent data and averaged diffusivity where multiple data sets are available.

Section 2 explains the data used and methodology. Of the 10 hydrographic sections, the meridional section nominally along 95°E is the only section visited three times with good quality CTD and LADCP data. In Section 3, we take advantage of this meridional section to study depth-latitude profiles of turbulence as well as internal wave properties. One issue we wish to address is the impacts of temperature diffusion and salinity diffusion on vertical density fluxes. Although our data sets are limited in temporal coverage, the weaker temporal than meridional (spatial) variability that we observed supports the contention of Kunze (2017) that the large scale geography of turbulence is repeatable. Encouraged by this finding, we plot a spatial map of turbulence for the entire Indian Ocean in Section 4. By using correlations between vertical diffusivity and topographic roughness and the input of wind power at near inertial frequencies, we are able to fill the gaps between observation sections (Section 5). It is then possible to follow up on the work of Huussen et al. (2012) by averaging the diapycnal diffusion and comparing the averages with the diapycnal fluxes required to explain the meridional overturning circulation across 32°S. The addition of new data did not change the conclusion that mixing driven by internal wave breaking estimated from these sections is insufficient to explain the meridional overturning circulation. Possible reasons are discussed in Section 6.

Throughout the work, we use an approximate neutral density of Jackett and McDougall (1997) where $\gamma^n = 28$ designates the isopycnal with a density of 1,028 kgm^{-3}. The equation of state for sea water is TEOS-10 (IOC & IAPSO, 2010).

2. Gregg-Henyey-Polzin Turbulence Parameterization

We use temperature and salinity data measured with CTDs and horizontal velocities measured with LADCPs. Most of these data were collected on cruises that were part of WOCE (World Ocean Circulation Experiment), CLIVAR (Climate and Ocean, Variability, Predictability, and Change) and GO-SHIP (Global Ocean Ship-Based Hydrographic Investigation Program). The cruises are listed in Table A1.

The CTDs and LADCPs used in these large-scale observation programs measure vertical scales of meters ("finescale"), which are larger than the turbulence dissipation scale ("microscale"), rather than measuring turbulence directly. To use these data to characterize the turbulence, we employ the "Gregg-Henyey-Polzin" parameterization documented by Polzin et al. (2014). The parameterization is based on the assumption of the steady energy balance wherein the spectral energy transport in the vertical wave number domain approximately equals the rate of turbulent kinetic energy dissipation. Considering heuristic constraints and a ray tracing model (Henyey et al., 1986), the spectral energy transport in terms of turbulent energy production in W kg^{-1} is expressed as follows:

$$P = 8 \times 10^{-10} \frac{f}{f_0} \frac{N^2}{N_0^2} \hat{E}^2 h\left(R_\omega, \frac{N}{f}\right), \tag{1}$$

where f is the Coriolis parameter, N^2 is the background buoyancy frequency, and R_ω is the ratio of horizontal kinetic (E_k) and potential (E_p) energy, that is,

$$R_\omega = \frac{\omega^2 + f^2}{\omega^2 - f^2} = \frac{2m^2 E_k}{2m^2 E_p}, \tag{2}$$

where m is the wavenumber. The frequency correction term h is given by

$$h\left(R_\omega, \frac{N}{f}\right) = \frac{\cosh^{-1}(N / f)}{\cosh^{-1}(N_0 / f_0)} \frac{3(R_\omega + 1)}{4R_\omega} \sqrt{\frac{2}{R_\omega - 1}}.$$

The background buoyancy frequency was estimated by a least squares fit of the second order polynomial to sorted 2-dbar buoyancy frequency measured by CTD. The subscript 0 means the standard value for the Garrett-Munk spectrum (f_0 at a latitude of 32.5° and $N_0 = 3$ cycles per hour). The shear spectrum $\hat{E}$ is evaluated as

$$\hat{E} = \frac{\int_{m_1}^{m_2} m^2 E_k(m) \mathrm{d}m}{\int_{m_1}^{m_2} m^2 E_k^{\mathrm{GM}}(m) \mathrm{d}m} \tag{3}$$

where E_k is the horizontal kinetic energy and the superscript GM means that for the Garrett-Munk spectrum. The lower wavenumber m_1 is the lowest wavenumber resolved and the higher limit m_2 is the highest below both the LADCP noise limit and "transition into wave-breaking regime," that is, largest wavenumber m_c satisfying

$$\int_{m_1}^{m_c} 2m^2 E_k(m) \mathrm{d}m \le 2\pi \frac{N^2}{10}. \tag{4}$$

The same wavenumber range (m_1, m_2) is used for the strain spectrum calculation. The spectrum calculation is performed using a Fast Fourier Transform with a Bartlett window at half-overlapping segments of 320 dbar length constructed upward from the bottom. The surface layer of thickness 500 dbar is excluded. The LADCP noise is estimated using the noise model of Polzin et al. (2002). We discard LADCP signals weaker than twice the noise level. We apply spectral correction to LADCP data using the correction coefficients from Polzin et al. (2002). For newer LADCP data processed with the inverse tool of Visbeck (2002), the correction coefficients from Thurnherr (2012) are applied.

Polzin et al. (2014) noted that the local and steady-state assumptions of the parameterization can be invalidated by factors such as nonlocal spectral transport (e.g., shear instability, low-vertical-mode resonant

interactions), boundary effects that short circuit downscale energy transfer (e.g., scattering and reflection of waves, viscous layer), and strong shear in the mean flow (e.g., fronts, equatorial currents, and topographic Rossby waves). It is difficult to estimate the uncertainty in the parameterization. Polzin et al. (1995) have demonstrated consistency between the parameterized and observed dissipation within a factor of 2. In Section 5 of Polzin et al. (2014), the parameterization yield estimates different from the microstructure estimates by a factor of 0.7–1.7 in most cases. In some cases, however, the parameterizations underestimate the microstructure observation by more than a factor of 5 (e.g., in a region dominated by staircase structures from double diffusion). In other cases, they overestimate them by a factor of 4–8 (e.g., under intense wave-mean flow interactions). Comparisons of turbulence measured by microstructure profilers and finescale parameterization have also revealed that the averaging depends strongly on the temporal and spatial scales (Whalen, 2021).

3. Spatial and Temporal Variability of Mixing Along 95°E

The I08°S–I09°N section, nominally along 95°E, was occupied three times in 1995, 2007, and 2016. The section runs from the low latitudes in the Northern Hemisphere to the high latitudes in the Southern Hemisphere across the Antarctic Circumpolar Current, and it covers smooth and rough topographies. Before discussing the geography of mixing on the basin scale, we study this particular section in detail. For comparison, another section from the western Indian Ocean, nominally along 55°E is shown in the Supporting Information (Figure S1).

3.1. Dissipation Rate

In Figure 1, we have plotted the turbulent kinetic energy dissipation rate ϵ, because this quantity is directly estimated by the parameterization and is also a measure of diapycnal density flux;

$$\langle \rho' w' \rangle = -K \langle \frac{\mathrm{d}\rho}{\mathrm{d}z} \rangle = -\frac{\rho_0}{g} \Gamma \epsilon, \tag{5}$$

that is, ϵ multiplied by the mixing efficiency $0 < \Gamma < 1$ is the diapycnal buoyancy flux, hence is flux associated with mixing.

Figure 1 shows horizontal structures found in all three occupations. The weak dissipation in low latitudes is expected from the vanishing Coriolis parameter in Equation 1 and smooth topography. Dissipation is strong over rough topography, namely, over the Broken Ridge (~30°S) and the Southeast Indian Ridge (around 45°S). The former might mask the possible enhancement of dissipation due to Parametric Subharmonic Instability of the semidiurnal tides at 28.9°S (Hibiya & Nagasawa, 2004; MacKinnon & Winters, 2005). Fronts embedded in the Antarctic Circumpolar Currents pass the southern flank of the Southeast Indian Ridge (the Subarctic and Polar Fronts are approximately at 48°S and 52°S in the climatological map of Orsi et al. (1995)). Vertically, the dissipation is strong near the pycnocline (depth of ~1,000 m) and decreases toward the bottom over smooth topography of the Bengal Fan north of 20°N. Near-bottom data are missing because velocity signals from the LADCP were below the noise level. In the 2007 occupation, enhancement over rough topography is apparent over the Southeast Indian Ridge. The reoccupations (in 2007 and 2016) of the I09°N section took place about 4° west in longitude of the original 1995 section such that it passed over the 90 East Ridge at about 7°N. Turbulence is enhanced over the ridge. In 1995, the sensor sensitivity of the LADCP sensor was lower than that of modern instruments, and the signal was below the noise level toward the bottom, except for the direct reflection from the bottom. The 2016 occupation suffered from lost and malfunctioning LADCPs (Macdonald, 2016).

3.2. Internal Wave Properties

The parameter R_ω in Equation 2 is the ratio of internal wave kinetic energy to internal wave potential energy, and is equal to the ratio of shear to strain. In the frequency domain, both kinetic and potential energies are weighted by their spectral power. If the internal waves are assumed to be locally dominated by one frequency ω (monochromatic wave assumption), the dominant wave frequency can be expressed by using R_ω;

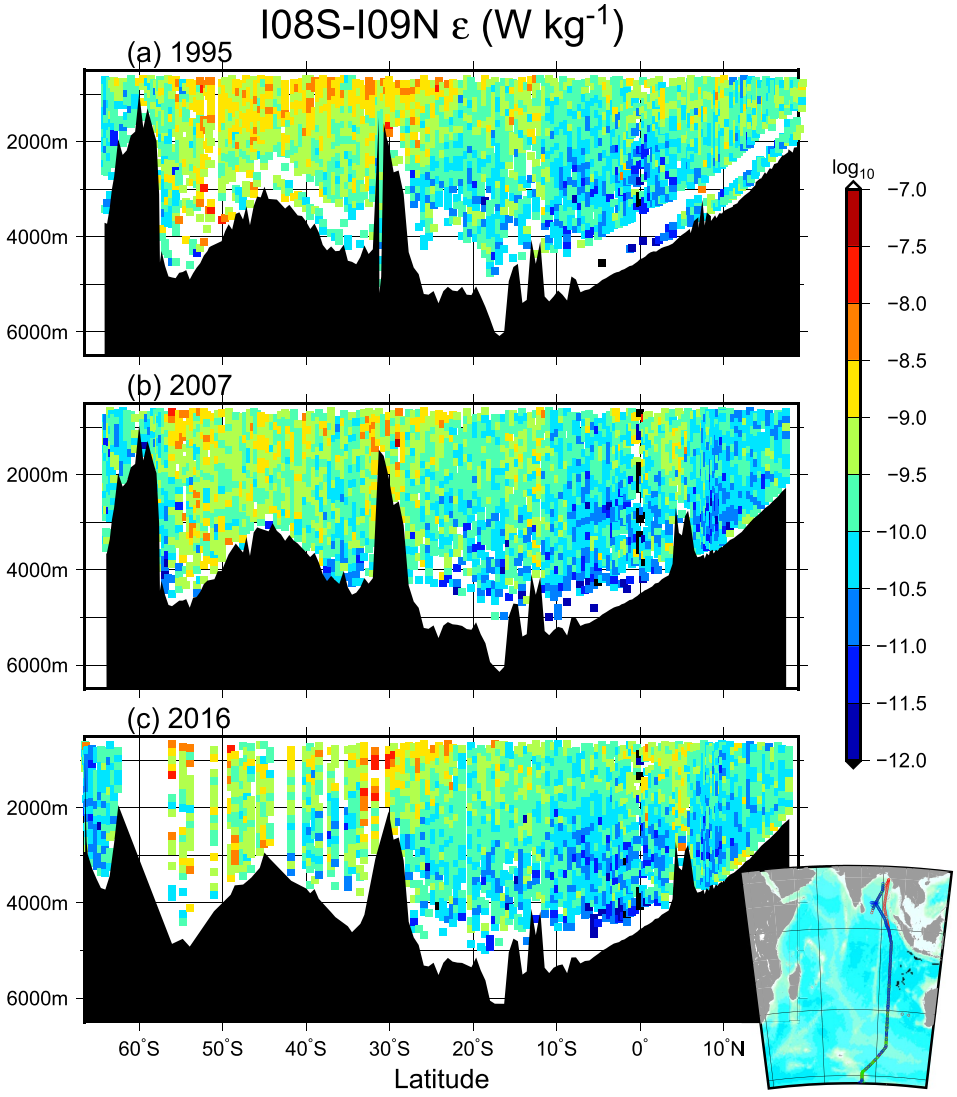

Figure 1. Turbulent kinetic energy dissipation estimated by finescale parameterization along the I08°S–I09°N section, nominally along 95°E in the Indian Ocean. The locations of the stations are shown in the right bottom inset. Some of the 1995 stations (red) and most of the 2007 stations (green) are overlapped by the 2016 stations (blue). The meridians are 30°, 60°, and 90°E and the latitudes are 0°, 30°, 60°S.

$$\frac{\omega}{f} = \sqrt{\frac{R_\omega + 1}{R_\omega - 1}}. \tag{6}$$

One can interpret ω/f as a measure of the contribution of near-inertial frequency waves relative to other higher-frequency waves (tides, harmonics of the tidal and inertial, etc.). Kunze et al. (2006) found that the mode and mean of R_ω are 6.1 and 10.6, respectively, which corresponds to $\frac{\omega}{f}$ = 1.18 and 1.10, respectively. A comparison of Figure 2 with Figure 1 shows that there is a tendency for high frequency to be correlated with strong mixing. The relationship is explained by the h term in Equation 1 as shown in Figure 10 of Polzin et al. (1995).

The rotary spectrum decomposition of the shear measured by the LADCP yields the energy of the clockwise and counter-clockwise velocity components. In the Southern Hemisphere, a stronger clockwise component than counter-clockwise component means downward phase propagation and upward energy propagation if

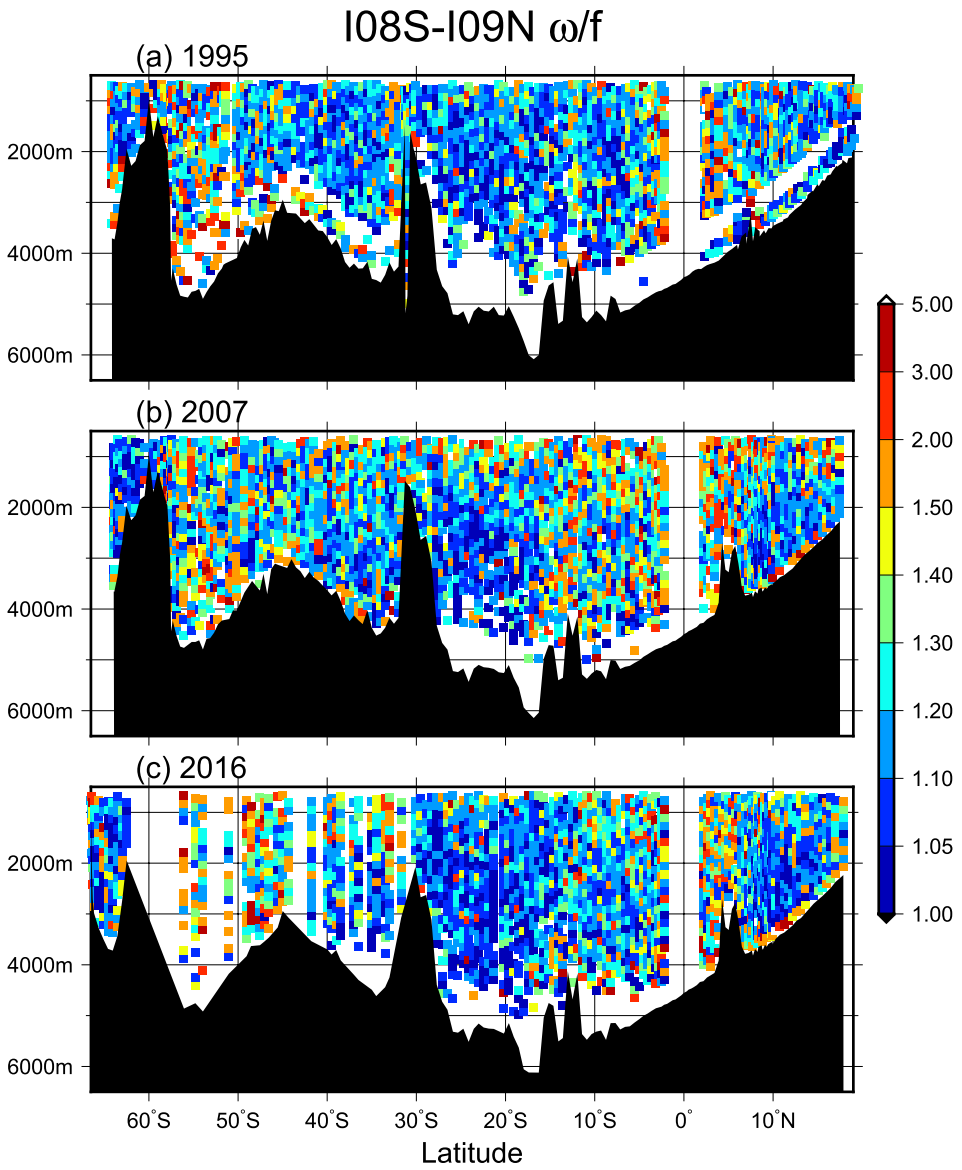

Figure 2. Based on the assumption of monochromatic internal wave dominance, the frequency of the wave ω divided by the Coriolis frequency f is shown along the I08°S–I09°N section. Note the nonlinear color coding. To avoid singularity at $f = 0$, data within ±2° off the equator are not plotted.

the wave is monochromatic. The shear spectra of the binned LADCP velocity are calculated with the Bartlett window to suppress spectral leaks. Shear levels lower than twice the LADCP noise model are discarded and only the wavelengths longer than the wavelength that corresponds to a transition to wave-breaking (Equation 4) are used. Figure 3 shows those data points associated with ratios of the clockwise and counter-clockwise components that are statistically different from zero based on the 95% confidence interval. Expecting that downward propagating waves are generated at the surface and upward propagating waves at the bottom, we use height above bottom as the vertical axis for the former and depth for the latter.

We find that energy propagates both downward and upward. The frequency is generally near inertial ($\omega/f < 1.3$). Most upward-propagating waves are found within 2,000 m from the bottom, a result not inconsistent with the assumption that they are generated at the bottom. Downward-propagating waves are found throughout the water column, but their detection only within 1,000 m from the bottom in some places suggests the possibility that they are generated locally through nonlinear interactions or that they are topographically driven waves that are generated nearby and propagating downward. The LADCP data

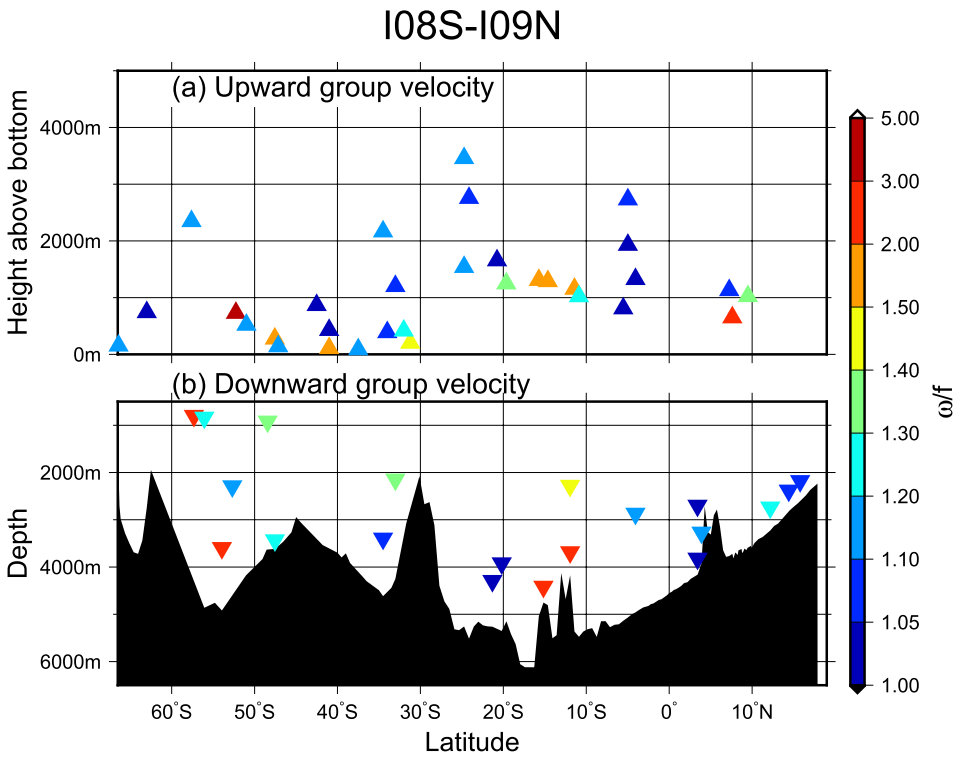

Figure 3. Distribution of bins (320 m length, half-overlapping) where statistically significant upward or downward group velocity were found on the I08°S–I09°N section. Vertical axis is height above bottom for top panels and depth for bottom panels. All occupations are plotted in one panel but the bottom topography for (b) was taken from the 2016 occupation. The color is the frequency of the internal wave on the assumption that the wave is monochromatic. To avoid singularity at $f = 0$, data within ±2° from the equator are not plotted.

are thus limited in number, accuracy, and resolution for purposes of demonstrating sources and sinks of internal waves.

3.3. Diapycnal Fluxes

In this subsection, the diapycnal fluxes are examined by assuming (a) the vertical diffusivities for density, temperature, and salinity are all equal (i.e., $K_\rho = K_T = K_S$) and (b) mixing efficiency $\Gamma = 0.2$ such that the vertical diffusivity is estimated as

$$K_\rho = \Gamma \frac{\epsilon}{N^2}.$$

Both the first (Gargett, 2003) and second (Ijichi et al., 2020) assumptions are debatable. The fluxes of heat and salt are converted to a flux of buoyancy using the thermal expansion coefficient α and haline contraction coefficient β, both of which are calculated for the bin-averaged temperature and salinity. We use the convention where $\alpha > 0$, and $\beta > 0$. The density change $\Delta\rho$ is therefore related to the changes of temperature ΔT and salinity ΔS by the equation $\Delta\rho = -\alpha\Delta T + \beta\Delta S$ on the assumption that higher-order terms are negligible. The diapycnal fluxes due to mixing of temperature T and salinity S are parameterized as follows

$$\langle T'w' \rangle = -K_T \frac{\mathrm{d}\langle T \rangle}{\mathrm{d}z} \tag{7}$$

$$\langle S'w' \rangle = -K_S \frac{\mathrm{d}\langle S \rangle}{\mathrm{d}z}, \tag{8}$$

where z is positive upward.

We start the discussion with the flux across the lower isopycnal $\gamma^n = 28.11$ (Figure 4b). This density is known as the bottom boundary of Circumpolar Deep Water (Robbins & Toole, 1997). Because the station-to-station differences of diffusivity are much larger than those of the temperature/salinity gradients ($\mathrm{d}\langle T, S\rangle/\mathrm{d}z$), the station-to-station differences of the diapycnal fluxes follow the spatial pattern apparent in Figure 1 – higher near topographic features and in the ACC. In low latitudes, the vertical temperature gradients of temperature and salinity are approximately 0.8°C per 1,000 dbar and 0.02 g/kg per 1,000 dbar, respectively. This contrast is somewhat compensated by the smaller magnitude of the thermal expansion ($\alpha \sim 1.6 \times 10^{-4}\mathrm{K}^{-1}$) versus the haline contraction ($\beta \sim 7.4 \times 10^{-4}\,(\mathrm{g/kg})^{-1}$). The result is that the contribution of the heat flux to the buoyancy is ~10 times the contribution of the salt flux. Within this density range, both background temperature and salinity increase toward the surface. The increase of salinity toward the Lower Circumpolar Deep Water (LCDW) salinity maximum (Figure 4c) causes the diapycnal fluxes of heat and salt to both be downward. At high latitudes, the $\gamma^n = 28.11$ isopycnal is shallower than 1,500 dbar, and the temperature and salinity gradients there are approximately 1.2°C and 0.1 g/kg per 1,000 dbar, respectively. Both temperature and salinity increase toward the surface.

The ratio of salinity flux to that of temperature is the inverse of the so-called density ratio R_ρ; ratio R_ρ;

$$\frac{\beta\langle S'w'\rangle}{-\alpha\langle T'w'\rangle} = \frac{\beta K_S \dfrac{\mathrm{d}\langle S\rangle}{\mathrm{d}z}}{-\alpha K_T \dfrac{\mathrm{d}\langle T\rangle}{\mathrm{d}z}} \tag{9}$$

$$= R_\rho^{-1} \tag{10}$$

which is conveniently expressed using the Turner angle (Figure 4d);

$$\tan T_u = \frac{1 - R_\rho^{-1}}{1 + R_\rho^{-1}}. \tag{11}$$

The Turner angle not only shows the relative ratio but also signifies the possible mixing status of the water column (Ruddick, 1983); for $|T_u| < 45°$, the water column is stable; for $45° < T_u < 90°$, salt fingering is possible; and for $-90° < T_u < -45°$ double diffusion is possible. The Turner angle along $\gamma^n = 28.11$ is about 50° and increases to about 65° south of 50°S (Figure 4d). Hence there is a potential for salt fingering to contribute to diapycnal mixing. This effect is not captured by the parameterization in Equation 1, but You (1999) has argued that this effect is an order of magnitude smaller than the turbulent diffusion for heat fluxes and and comparable for salt fluxes.

Whereas the salinity flux is always downward (upward buoyancy) across $\gamma^n = 28.11$, it changes to upward (downward buoyancy) south of about 15°S across $\gamma^n = 28.0$ (Figure 4a). The upward salinity flux (downward buoyancy flux) increases southward and its impact on mixing becomes comparable in magnitude to that of the temperature flux as a result of increased vertical salinity gradient (Figure 4a). At 50°S, the isopycnal $\gamma^n = 28.0$ is about 1,800 m deep, above the salinity maximum of LCDW (Figure 4c). The salinity flux is therefore upward and is associated with a salinity gradient of ~0.1 g/kg per 1,000 dbar. This sign change is a result of a change of sign of the background salinity stratification; south of ~15°S, the salinity minimum of Antarctic Intermediate Water (AAIW) is centered around 1,000 m (Figure 4c). Along 95°E, south of the Broken Plateau (South Australia Basin), there is a salinity maximum of LCDW due to advection of salty Atlantic Ocean water at a depth of ~2,500 dbar (Figure 4c). These water masses shoal toward the surface southward and AAIW outcrops at the Subantarctic front at ~45°S. LCDW approaches the surface but does not outcrop, at least in summer. As a result, the isopycnal $\gamma^n = 28.0$ being the upper limit of LCDW is in a region where salinity stratification decreases toward the surface south of ~15°S.

In this section, we consider the difference in diapycnal mixing associated with temperature and salinity. The salinity contribution changes sign, and the fluxes associated with temperature and salinity gradients become comparable in the polar regions south of 30°S. The flux estimates, however, are associated with

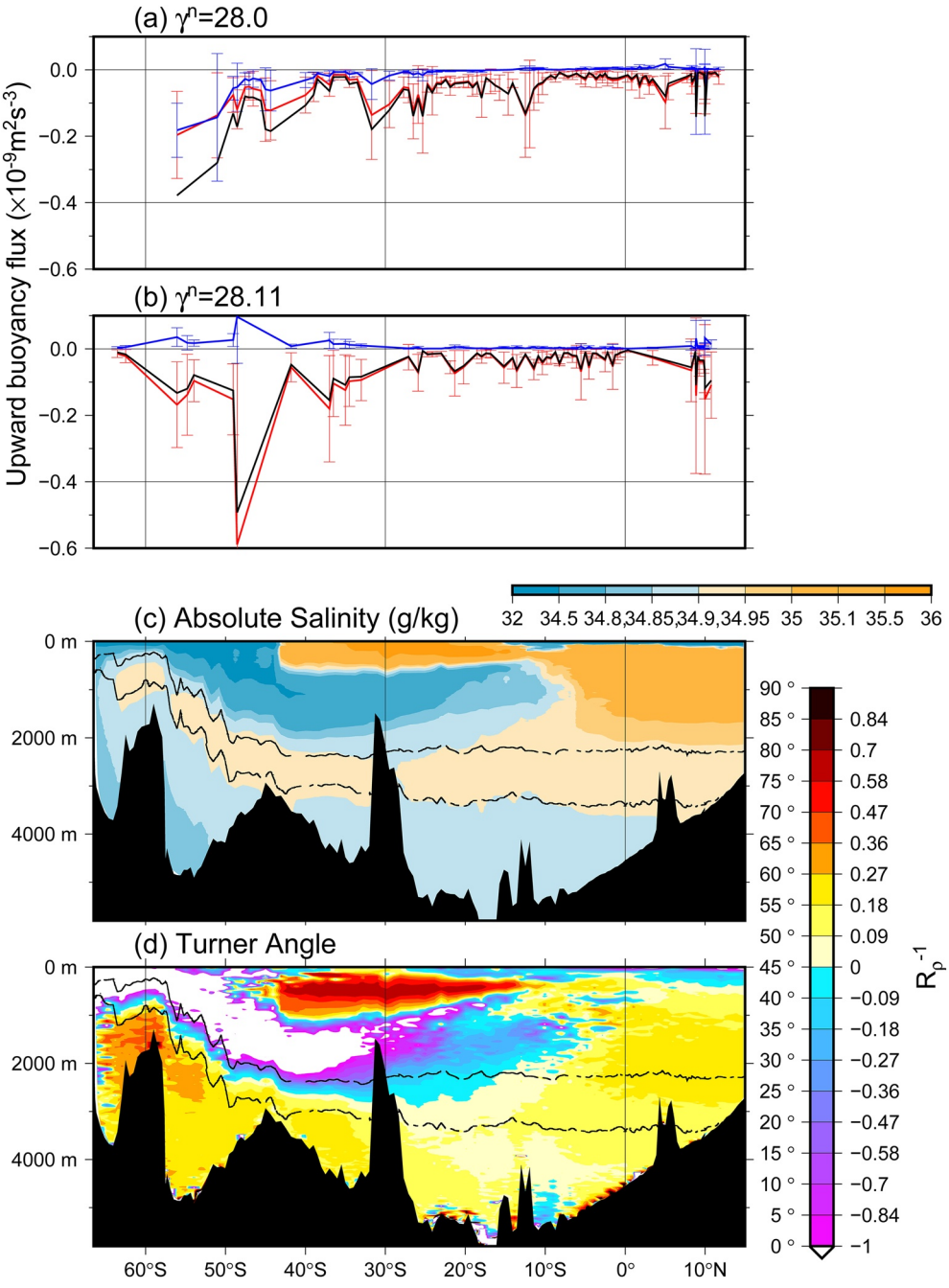

Figure 4. (a) Diapycnal flux of buoyancy $-g\rho/\rho_0$ due to mixing of temperature (red), salinity (blue) and the sum (black) across the neutral density surface $\gamma^n = 28.0$ along the meridional section I08°S–I09°N; (b) the same quantities for $\gamma^n = 28.11$; (c) Absolute Salinity; and (d) Turner angle and corresponding inverse density ratio R_ρ^{-1}. The hydrographic data and bottom topography for (c) (d) were taken from the 2016 occupation. The thin vertical lines show the latitudes of 0°, 30°, and 60°S. The thick lines in (c) and (d) show the location of the isopycnals $\gamma^n = 28.0$ and 28.11. The fluxes are calculated as diffusivity estimated by Equation 1 multiplied by the vertical gradient of temperature and salinity measured by CTD. The average over three occupations is plotted with the standard deviation shown by the error bars.

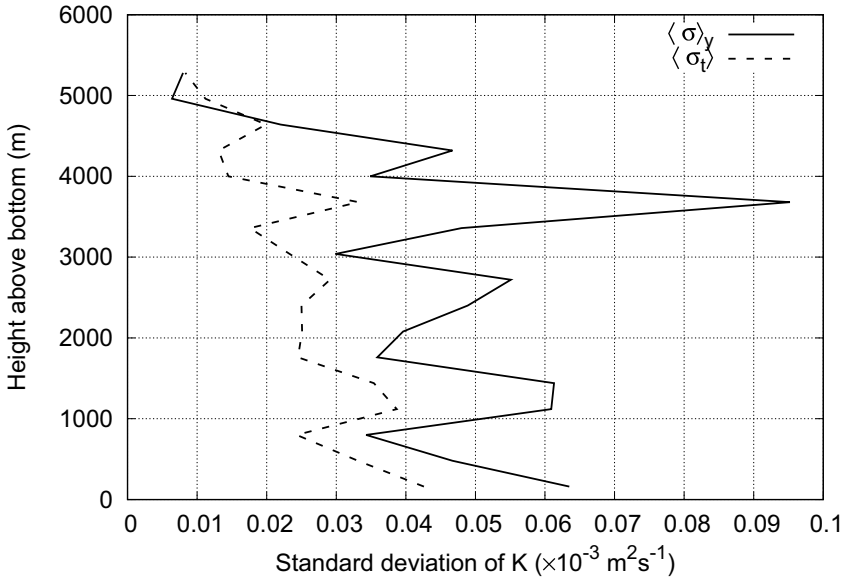

Figure 5. Standard deviation σ of diffusivity K along the I08°S–I09°N section. The dashed line shows average of temporal standard deviation σ_t for all stations within the same depth bin. The solid line shows latitudinal standard deviation of temporal means $m^{(j)}$ in Equation 12.

a large uncertainty because of the large variability of turbulent mixing. We also note the tendency for salt fingering to increase in the polar region for $\gamma^n = 28.11$. This tendency adds a mechanism for diapycnal mixing distinct from turbulence, and is potentially important for the salt flux (You, 1999). Mixing affected by nonlinearity in the equation of state of seawater (cabbelling and thermobaricity) is also important in this region (Klocker & McDougall, 2010) but cannot be captured by the parameterization in Equation 1.

3.4. Spatial and Temporal Variabilities

The I08°S–I09°N section is the only section occupied three times where we can estimate temporal variation of vertical diffusivity K. At a station j, temporal standard deviation σ_t of K is estimated from the three occupations. Stations within 0.2° in both longitude and latitude are considered to be station j.

$$m^{(j)} = \frac{K_{1995} + K_{2007} + K_{2016}}{3}$$
$$(\sigma_t^{(j)})^2 = \frac{(K_{1995} - m^{(j)})^2 + (K_{2007} - m^{(j)})^2 + (K_{2016} - m^{(j)})^2}{2} \quad (12)$$

Our choice of an arithmetic mean in Equation 12 rather than an average based on a fit to lognormal distribution for K is justified in Appendix C. Throughout this calculation, we assume a mixing efficiency $\Gamma = 0.2$. The depth bin is 320 m, which is the same bin length as used in the finestructure parameterization 1. The spatial variation is quantified as variation of the temporal means $m^{(j)}$ for all j from 65°S to 19°N.

Figure 5 shows that at all depths within 4,700 m of the bottom, spatial variability $\langle\sigma\rangle_y$ is larger than temporal variability $\langle\sigma_t\rangle$. If this relationship holds on other sections, spatial variation is generally larger than temporal variation. It is therefore a meaningful exercise to plot the diffusivity for all sections on one map to study the spatial characteristics of the diffusivity even though some section has been occupied only once.

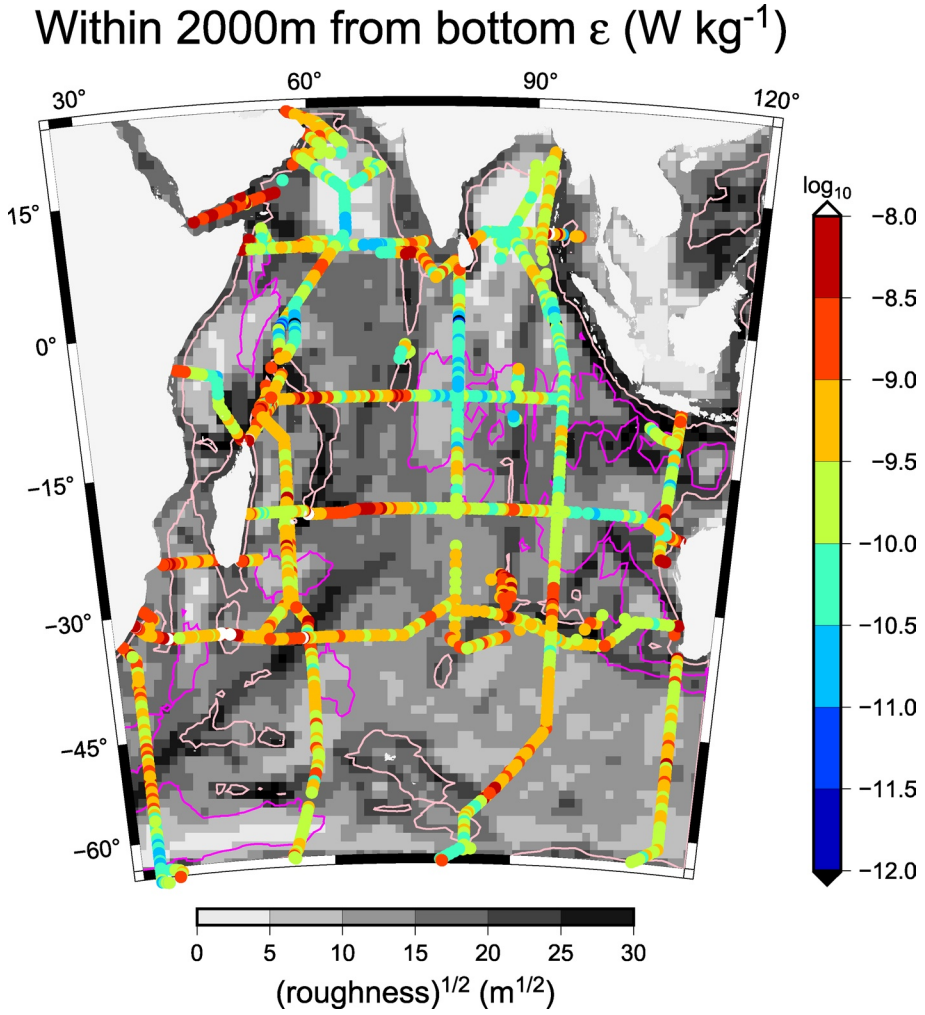

Figure 6. Turbulent kinetic energy dissipation rate (ϵ in W kg^{-1}) averaged within water columns from the bottom to 2,000 dbar above the bottom. Rates are shown in the logarithmic scale to base 10. The pink contours show the 2,500 m-depth isobath and the magenta contours show the 5,000 m-depth isobath. The gray shading shows the roughness (defined in the main text). For sections occupied two or three times (Table A1), arithmetic averages are used.

4. Dissipation Rate ϵ and Internal Wave Frequency ω in the Indian Ocean

All available section data are aggregated to examine the horizontal structure of the diapycnal mixing. Decloedt and Luther (2010) proposed a vertical profile of diapycnal diffusivity as a function of the height from the seabed z having a form of

$$K \sim \left(1 + \frac{z}{h_0(R)}\right)^{-2}, \tag{13}$$

where the values of the scale height $h_0(R)$ estimated from 273 near-bottom, in situ microstructure observation were weakly related to topographic roughness, R, and most of them were less than 2,000 m (Figure 6b of Decloedt & Luther, 2010). We therefore use a vertical average within 2,000 m of the seabed to represent the dissipation in the water column. We plot the kinetic energy dissipation rate Equation 5 as we did in Figure 1.

Figure 6 shows the horizontal distribution of turbulence. The dissipation shows peaks ($\epsilon > 10^{-9}$ Wkg^{-1}) at rough topographies ((roughness)$^{1/2} > 20$ m). We find less turbulent regions in smooth (the Bay of Bengal and the Arabian Sea, north of 10°N) and deep eastern basins.

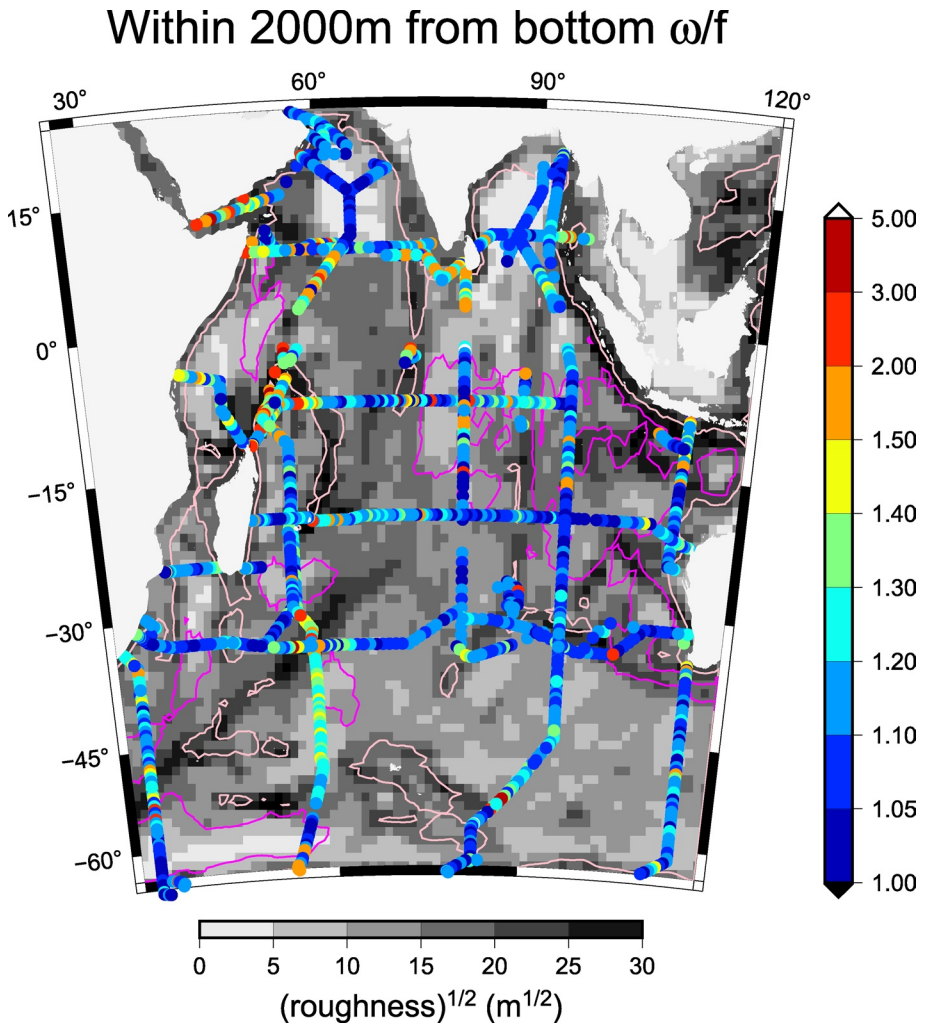

Figure 7. Frequency of the internal wave ω divided by the Coriolis frequency f. The pink contours show the idobath at a depth of 2,500 m, and the magenta contours show the isobath at a depth of 5,000 m. The gray shading shows the roughness (defined in the main text). Near equator estimates (within ±2°) are excluded.

Next, we average the internal wave frequency ω/f in Equation 6 within 2,000 dbar of the seabed (Figure 7). In many sections, internal waves tend to become more inertial with distance from rough topography, for example, (30°E, 50°S) over the Southwest Indian Ridge; (80°E, 55°S) over the Kerguelen Plateau; and (90°E, 10°N) over 90 East Ridge. This tendency is also discernible in Figure 2 around 15°S over the 90 East Ridge. It is noteworthy, however, that the tendency is not obvious over the Broken Plateau at 30°S and is thus probably not universal. Chinn et al. (2016) reported a similar tendency for waves emitted from the Hawaiian Ridge. There is an increase in R_ω (i.e., more inertial under the monochromatic assumption), as they propagate away, which was a result of decreasing strain energy and constant or increasing shear energy. Chinn et al. (2016) have also reported a counterexample where internal waves propagating offshore from the Oregon Coast did not show a simple trend in R_ω, likely because of its complex generation and propagation physics.

5. Parameterization of Diffusivity as a Function of Roughness and Wind

In this section, we attempt to extrapolate the estimated diffusivity K (Figure 6) to the entire Indian Ocean through a parameterization. We call the quantity estimated from observed hydrography and LADCP such as ϵ in Figure 6 "observed" and those extrapolated through a parameterization "estimated" parameters, although the former parameters are estimated via Equation 1.

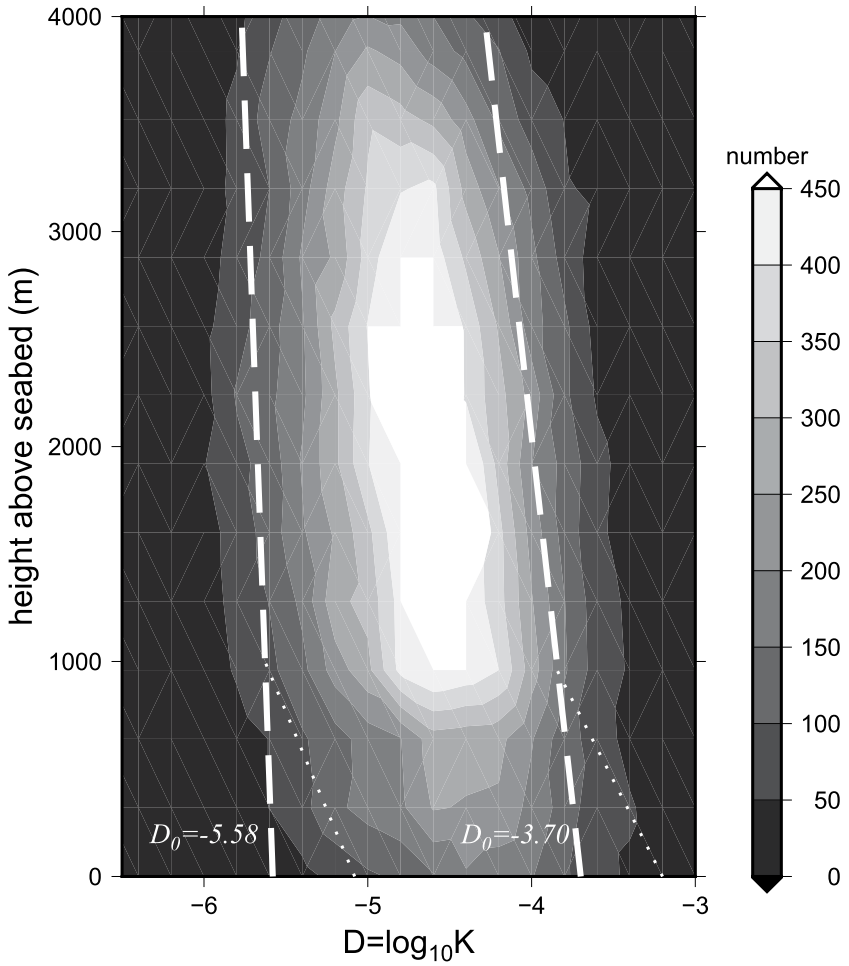

Figure 8. Distribution of diffusivity κ for all stations. The number of data within a box of 0.2 (horizontal) by 320 m (vertical) is shown by shading. Dash-dot lines representing the observed profile of diffusivity are shown for $D_0 = -5.58$ and $D_0 = -3.70$. See text for the definition of D_0. Dotted line near the bottom shows the bottom boundary model profile used in Section 6.2.

5.1. Vertical Profile of Diffusivity *K*

Polzin et al. (1995) have remarked that diffusivity K is more statistically stationary with depth than dissipation rate ϵ because ϵ scales as $\epsilon \sim E^2N^2$ where E^2 is the internal wave shear energy (Equation 3). Decloedt and Luther (2010) have compiled dissipation rates measured by microstructure profilers and have proposed a roughness diffusivity model;

$$K_\rho(z,R) = K_b(R)\left[1+\frac{z}{h_0(R)}\right]^{-2} + K_{\text{back}}, \tag{14}$$

where the boundary diffusivity $K_b(R)$ and scale height $h_0(R)$ are functions of the topographic roughness R, z is the height above the seabed, and K_{back} is the background diffusivity. The functions $h_0(R)$ and $K_b(R)$ were found by a nonlinear least squares fit to the observed data and described by a third-order polynomial and an exponential function of a third order polynomial, respectively.

Figure 8 shows the vertical distribution of the diffusivity K observed with Equation 1.The fact that the parameterization is associated with an uncertainty of a factor of five or so, as noted in Section 2, means that our data do not resolve features such as the curvature of the functional relationship (e.g., Equation 14). We thus fit a simpler linear function in logarithmic space instead (Figure 8). We also note that within 1,000 m

of the bottom, the number of data points decreases because the LADCP reflections were poor, particularly in the 1995 occupations (e.g., Figure 1a). We performed a least squares fit to a line segment between 1,000 and 3,000 m above the seabed. Let $D = \log_{10}K$ be the horizontal and z be the vertical axis in Figure 8, the lines of estimated diffusivity are defined as the lines that always pass through a fixed point ($D^* = -6.31$, $z^* = 15{,}246$). With a gradient α, the diffusivity profiles are then estimated as

$$z = \alpha(D - D^*) + z^* \tag{15}$$

When this profile is evaluated at the bottom $z = 0$,

$$D = D_0 = D^* - z^* / \alpha. \tag{16}$$

We use D_0 as the key parameter representing the diffusivity at one station. Once D_0 is determined, the diffusivity profile is calculated by Equation 15 by using α from Equation 16.

5.2. Environmental Parameters Potentially Affecting the Vertical Diffusivity

Scatter plots were used to visually examine the relationships between the diffusivity, quantified by D_0 and environmental parameters. The environmental parameters considered are roughness, wind power input at near-inertial frequencies, wind power input via the geostrophic surface velocity, mesoscale eddy kinetic energy, and near-bottom velocity.

5.2.1. Topographic Roughness

It has been demonstrated (e.g., Decloedt & Luther, 2010; Huussen et al., 2012) that turbulence depends on the roughness of the bathymetry. In accord with the definition used in Huussen et al. (2012), we equated bottom roughness to the mean square distance between a smooth second order polynomial fit and the Smith and Sandwell bathymetry (Becker et al., 2009) within a 0.5° × 0.5° rectangle. The gray shading in Figure 6 shows the roughness.

5.2.2. Wind Input at the Inertial Frequency

The input of wind power at the inertial frequency was estimated with the slab model as described in Appendix B. Alford and Whitmont (2007) have demonstrated winter enhancement of near-inertial energy in the mid-latitude Northern Hemisphere at depths greater than 3,000 m. The variability closely follows that of the wind-forced, near-inertial mixed-layer energy flux estimated by a slab model. Although the seasonal signal is not as clear in the Southern Hemisphere, the peaks in the kinetic energy at depths down to 4,000 m at a seasonal-to-subseasonal time scales corresponded with those in the mixed-layer wind energy flux (their Figure 5). The phases of the seasonal variations of the kinetic energy and wind energy flux suggest that the wind forcing penetrates to depths as great as 4,000 m in less than 100 days. Gill (1984) used a set of vertical normal modes to show theoretically that although the near-inertial energy is mostly confined to the near-surface layers, some energy injected by the wind into the mixed layer penetrates more than 4,000 dbar within a time frame on the order of days (his Figure 4). This is the contribution from the gravest vertical modes and is consistent with an estimated based on ray theory of the travel time from the mixed layer to the bottom by Garrett (2001); 8.3j days at latitude 30° for vertical mode j in the limit of a large horizontal scale. For layers shallower than 2,000 m, Whalen et al. (2018) have assumed that the near-inertial energy propagates downward at a velocity of 10–17 m per day based on the results from data taken in the upper 800 m of the water column (Alford et al., 2012), that is, without the gravest few modes. In deep (>2,000 m) layers, the travel time for these high-mode waves exceeds the time nonlinear wave-wave interactions grow until they are no longer negligible in magnitude (McComas & Müller, 1981). We therefore expect that the gravest few modes penetrate into the deep ocean and assume that such waves generated by the surface wind 10–80 days prior to the observation can potentially affect the turbulence in the deep ocean. Garrett (2001) has also estimated the meridional distance that wave packets travel from the surface to the first contact to the bottom (his Figure 2) at about 400 km. We therefore integrate the wind forcing in a circle around the CTD/LADCP station with a radius of 500 km.

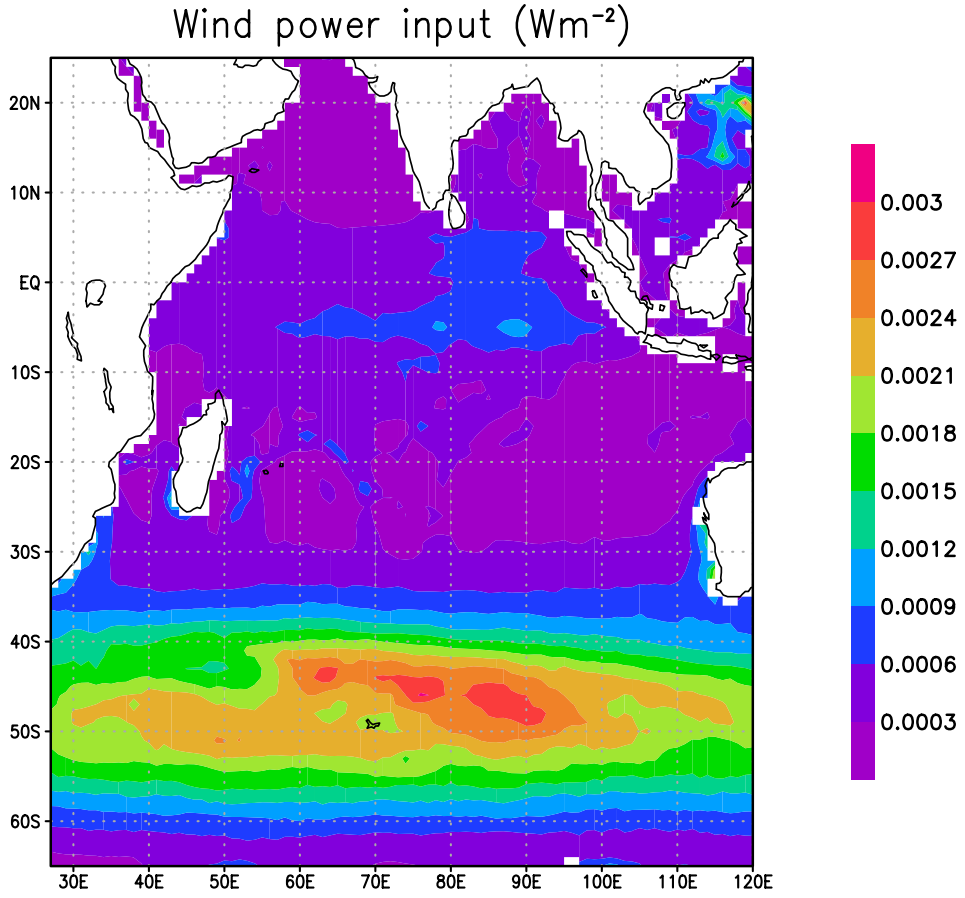

Figure 9. Power input from wind at near-inertial frequencies calculated with a mixed-layer slab model.

The input of wind power is large at high latitudes under the westerly jet and in equatorial regions where winds oscillate seasonally (Figure 9). We note that ship-based observations can be biased toward calm conditions and therefore could miss high-energy events.

5.2.3. Other Parameters

The fact that mesoscale eddies interact with near-inertial internal waves (Kunze, 1985; Polzin & Lvov, 2011) is related to the input of wind power at the near-inertial frequencies. In particular, anticyclonic eddies are conduits for the downward propagation of near inertial waves. Whalen et al. (2018) have demonstrated this property using an array of floats in the mid-latitude Northern Hemisphere. We estimate mesoscale eddy kinetic energy from the gridded altimeter product by assuming geostrophic balance. Our data, however, did not reveal a clear relationship between eddy kinetic energy and diffusivity. We note that the finding of Whalen et al. (2018) is for regions where wind input and eddy kinetic energy are both strong and we cannot expect that the relationship holds for the entire Indian Ocean, including regions of weak wind and eddy energy.

We also use the geostrophic velocity estimated from the gridded sea surface height in estimating the wind power input via the geostrophic surface velocity $\vec{v}$ as $\vec{\tau} \cdot \vec{v}$ where $\vec{\tau}$ is wind stress. This quantity does not show an obvious relationships with mixing.

Near-bottom velocity measured by LADCP is not correlated with dissipation or with diffusivity.

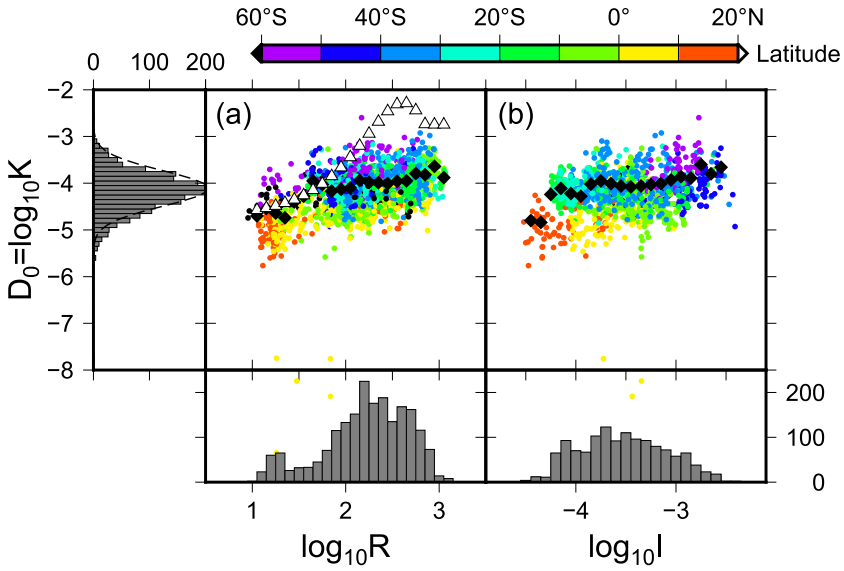

Figure 10. Distribution of diffusivity at seabed, D_0 in Equation 16, for all stations as function of (a) topographic roughness R and (b) wind power input at inertial frequency (i) Both axes are plotted on a logarithmic base 10 scale. Color shows the latitude of the observed station. Note that sample points outside of the panel were not cropped (e.g., several points from stations between 0° and 10°N are overlapping histograms (a) of $\log_{10}R$). This is done to confirm that no outlier with large D_0 contaminates the averaging procedure. Number of samples in D_0, $\log_{10}R$, and $\log_{10}I$ are shown in histogram with a bin size of 0.1. The black diamonds show the average in each roughness/wind power bin, calculated as $\log_{10}\langle 10^{D_0}\rangle$ where $\langle\cdot\rangle$ is arithmetic averaging. The white triangles in (a) indicates the roughness parameterization byDecloedt and Luther (2010) evaluated at the sea floor with the caveat that their definition of roughness is different from ours.

5.3. Correlation With Roughness and Wind

Figure 10 shows the relationship between the vertical diffusivity and topographic roughness and the input of wind power. Superimposed over the scatter plot of topographic roughness is the output of the roughness diffusivity model (Equation 14) of Decloedt and Luther (2010) evaluated at the seafloor. Note that their vertical profile (Equation 13) and definition of roughness differed from ours; they use a 4-term polynomial with a constant, x, y, and xy; we use a 5-term polynomial with a constant, x, x^2, y, and y^2. Figure 8 shows that the parameterization Equation 1 seldom produced values larger than $10^{-3}\mathrm{m}^2\mathrm{s}^{-1}$, while there was a peak greater than $10^{-3}\mathrm{m}^2\mathrm{s}^{-1}$ in the roughness diffusivity model at 300 m $< R <$ 500 m.

Because of the correlations between D_0 and $\log_{10}R$ and between D_0 and $\log_{10}I$, we define D_0 as a function of $\log_{10}R$ and $\log_{10}I$, that is,

$$D_0 = f(\log_{10} R, \log_{10} I). \tag{17}$$

The function f is assigned a value by table lookup. At the seabed $z = 0$, Equation 16 shows that $K = 10^{D_0}$. Through this exercise, we attempt to estimate mixing which is relevant to the meridional overturning circulation, hence to decadal and longer timescales. The long-term average $\langle\cdot\rangle$ of the mixing term in the governing equation for a tracer (say, Θ) is

$$\left\langle \frac{\partial}{\partial z} K \left(\frac{\partial}{\partial z} \Theta \right) \right\rangle = \frac{\partial}{\partial z} \left(\langle K \rangle \frac{\partial}{\partial z} \langle \Theta \rangle \right)$$

where K and Θ are assumed to have no correlation with time. In the lookup table used to assign values to f, all sample of D_0 are divided into groups defined by the arguments $\log_{10}R$ and $\log_{10}I$. The fact that the resolution of the arguments is 0.2 gives groups with zero to 64 members (average member size is 11.9) for $\log_{10}R$ = 1.0, 1.2, ..., 2.8 and $\log_{10}I$ = −4.4, −4.2, ..., −2.6. Each group is represented by $\log_{10}\langle 10^{D_0}\rangle$

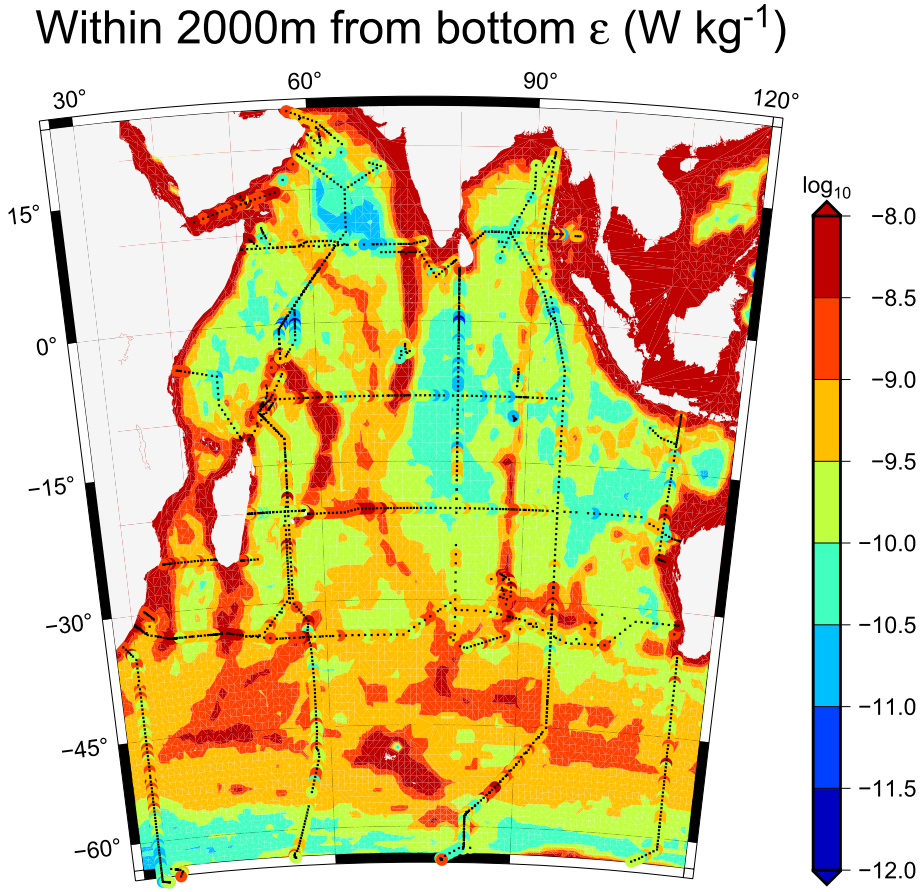

Figure 11. Estimated turbulent kinetic energy dissipation rate (ϵ in W kg^{-1}) averaged within water columns from the bottom to (bottom − 2,000 dbar) shown in a logarithmic scale on a 1° × 1° grid. The black crosses show the observed ϵ (the same quantity as shown in color in Figure 6) plotted over our estimation.

rather than $\langle D_0 \rangle$, where $\langle \cdot \rangle$ is the ensemble mean. Note that for ease of visualization, Figure 10 shows 2 two-dimensional scatter plots, one for $\log_{10} R$ and the other for $\log_{10} I$, but in the table lookup we use one table with two inputs ($\log_{10} R$ and $\log_{10} I$) and one output D_0 which would require a three-dimensional plot for illustrative purpose.

5.4. Estimated Diffusivity

Figure 11 shows the application of Equations 15 and 17 to the Indian Ocean using topographic roughness (Figure 6) and the time-averaged wind power input field (Figure 9).

On top of the estimated dissipation, we plot observed dissipation (the same quantity as shown in Figure 6). If the parameterization succeeds, the observed points are not distinguishable from the background color shade. The estimation reproduces the general features of the observed data (indicated by black crosse on Figure 11) but there are some mismatches in low-turbulence regions (e.g., along 80°E around the equator) and high-turbulence regions (e.g., over the Southern Ocean).

Figure 12 shows the estimates in the vertical section. The parameterization overestimates the diminished turbulence near the equator, as well as the low turbulence between 30°S and 40°S. The Supporting Information provides estimates of the diffusivity (D_0 and K) in a region bounded by 27°–120°E and 65°S to 25°N.

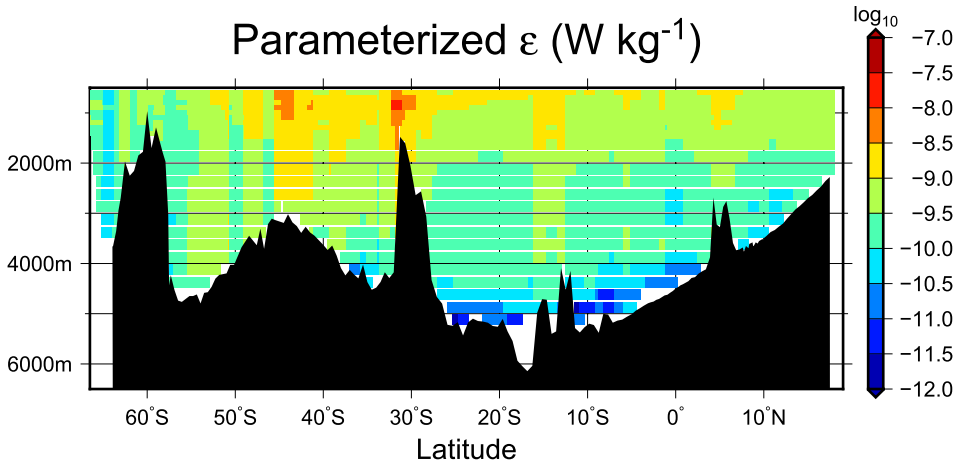

Figure 12. Estimated turbulent kinetic energy dissipation rate (ϵ in W kg^{-1}) along the I08°S–I09°N section. Compare with Figure 1. The station locations in the 2007 visit are used.

5.5. Is the Indian Ocean Meridional Overturning Circulation Driven by Internal Wave Breaking?

The parameterized mixing field (Figures 11 and 12) is interpolated onto neutral density surfaces calculated from the WOCE gridded climatological temperature and salinity data (Gouretski & Koltermann, 2004) and integrated north of 32°S. The result is plotted over the summary plot of Huussen et al. (2012).

The uncertainty due to sampling was estimated by averaging 10,000 resampled data; for each grid with roughness R and wind input I, a value of D_0 was sampled randomly from $f(\log_{10}R, \log_{10}I)$ (Equation 17) then this sampled values for all grids were averaged over the Indian Ocean north of 32°S for each isopycnal.

Most of the averaged dissipation rates are greater than the estimates by Huussen et al. (2012), except for density layers lighter than $\gamma^n = 26.94$, but they were not large enough to explain the Indian Ocean meridional overturning circulation (Figure 13a). We examine the effect of wind input by estimating the dissipation with $f(\log_{10}R)$ in Equation 17, that is, by assuming that the mixing depends only on roughness and not on inertial wind power input (figure not shown). The result is slightly (less than 10% in median value) smaller than the estimates with $f(\log_{10}R, \log_{10}I)$ and visually indistinguishable from Figure 13a. A short answer for the question raised in the section title is therefore "only partly if the GHP parameterization (Equation 1) and our interpolation (Equation 17) are perfect." We discuss the discrepancy in the next section.

6. Discussion

We updated Huussen et al. (2012) with recent data and with the surface power input from the wind at near-inertial frequencies (Figure 10). These improvements did not change their conclusion that the locally observed mixing (red and black crosses as well as rectangles in Figure 13a) is not sufficiently strong to explain the mixing required by the meridional overturning circulation (colored diamonds). Here we discuss possible explanations for the discrepancy.

6.1. Undersampling

The volume of the Indian Ocean north of 65°S between 27° and 120°E longitude is approximately 2.5×10^{17} m^3. Our data at ~2,000 stations, cover only a tiny fraction of this volume. The horizontal length scale of mixing is probably a complicated function of stratification, topography, surface forcing, etc, but we use a decorrelation scale for decadal temperature change of 163 km, as estimated by Purkey and Johnson (2010). Likewise, we use the vertical bin size of 320 m in the parameterization (Equation 1) as the vertical scale of mixing. These lengths are probably upper bounds. For example, D'Asaro and Perkins (1984) have observed a horizontal scale of internal wave at ~20 km; Yamazaki and Lueck (1990) have reported a vertical thickness scale of 8 m for a turbulence patch. For the temporal scale, we take 10 days as the decorrelation scale of mixing. Again, this is

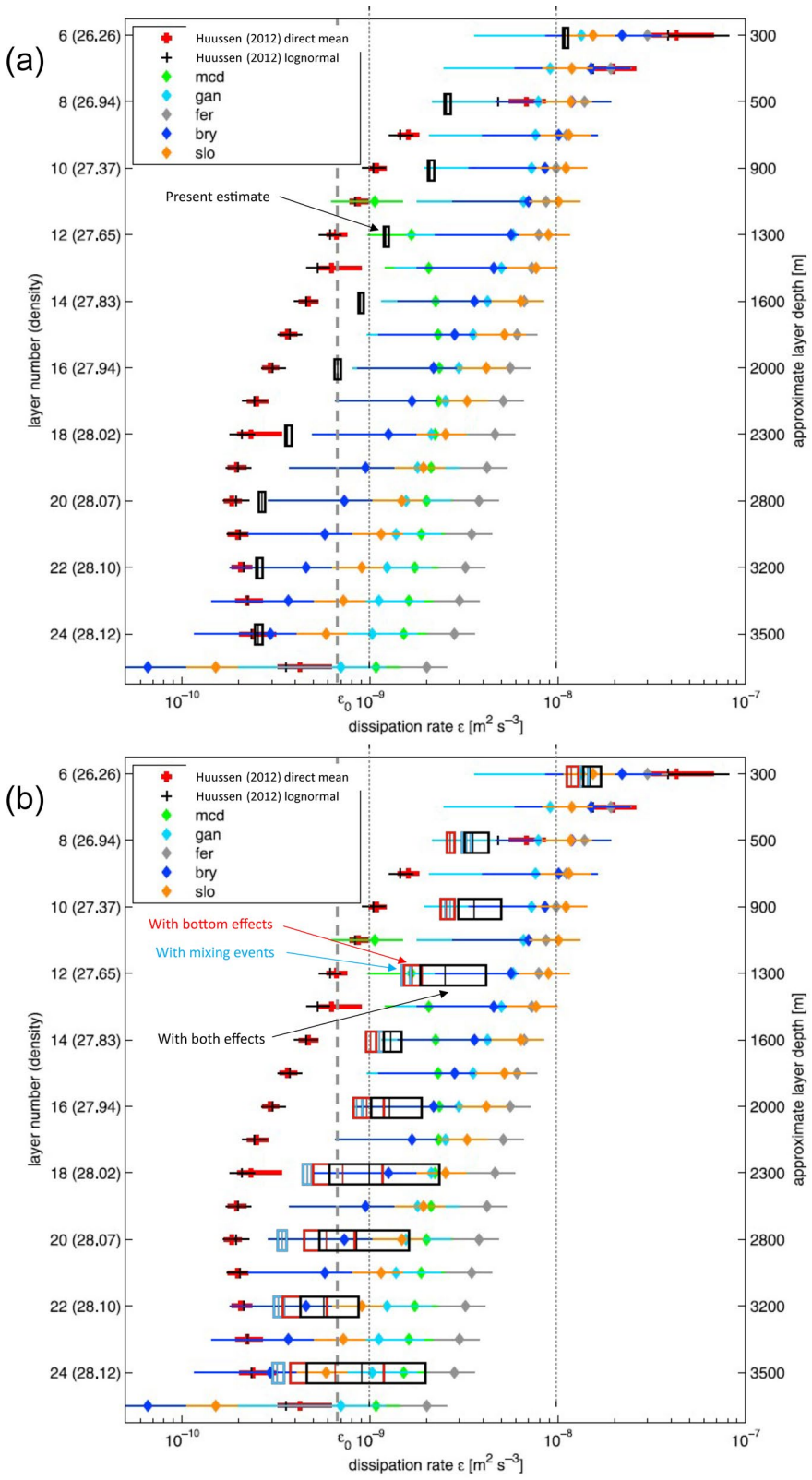

Figure 13

likely an upper bound given the dominant inertial, tidal, and overturning frequencies in the spectrum. With these spatial and temporal scales, our data spanning a duration of 25 years between 1995 and 2020 cover

$$\frac{2000 \times (163 \times 10^3)^2 \times 320 \times 10}{2.5 \times 10^{17} \times (25 \times 365)} \approx 1 \times 10^{-4}$$

of the mixing field. This estimate is also very optimistic. Given this tiny coverage and the bias caused by ship-based observations which can only collect data under calm-to-moderate conditions, it is quite possible that our data miss high-mixing events.

The tendency for internal waves with high frequencies to be rapidly dissipated (Figures 1 and 2) can be partially explained by the contribution from internal tides, which have frequencies higher than inertial frequencies. Because CTD stations are randomly timed relative to tides, they are likely to miss large-internal-tide events. Internal tides are generated over rough topographies and the waves, which have low vertical modes, propagate in beams (e.g., Arbic et al., 2010), the propagation of which depends on oceanic conditions such as horizontally varying stratification and are thus unsteady. For example, Waterhouse et al. (2018) observed that the tide beams in the Tasman Sea carried mode-1 semidiurnal energy fluxes that varied from <2 to >10 kWm^{-2} over the 55 day observation period. Some beams are dissipated on the continental slopes. Waterhouse et al. (2014) have estimated that as much as 31% of the power input from winds and tides may be dissipated on continental slopes. The hydrographic sectional observations used in this paper do not sample the continental slopes well.

Here we attempt to quantify these unobserved mixing events. Close examination of Figure 10 reveals a high-mixing event with $D_0 = -2.60$ at $\log_{10}R = 2.17$ and $\log_{10}I = -2.77$. This high mixing was observed during 316N145_5 cruise at (52.25°S, 88.30°E) on December 20, 1994. In the table lookup (Equation 17), $f(\log_{10}R = 2.17, \log_{10}I = -2.77) = -3.61$. This event was therefore $\Delta = -2.60 - (-3.61) = 1.01$ stronger in logarithm (i.e., roughly 10 times) than the table lookup value. If we assume that our observations missed high-mixing events with strength Δ stronger than the lookup value in each table entry for f in Equation 17, the averaged dissipation increases by a factor of 1.3–1.4 (Figure 13b, cyan rectangle).

Ocean current velocity field does not follow a normal distribution (Bracco et al., 2000). The kurtosis of the distribution is larger than that of a normal distribution, and hence extreme velocities are observed more frequently than if the velocity followed a normal distribution. If mixing follows a distribution in the logarithmic space with a kurtosis higher than that of a normal distribution, then the likelihood of high-mixing events is greater than expected from a normal distribution. It is possible that we missed these events. Because our estimates are sensitive to these high-mixing events, addition of a few high-mixing data points could easily explain the gap between the observed and parameterized dissipation (Figure 13b). Yamazaki et al. (1990) have provided an example of how undersampling turbulence observation can result in a large difference in average dissipation.

6.2. Near Bottom Processes

The parameterization in Equation 1 does not capture mixing events such as scattering and reflection of internal waves, topographic lee waves, and hydraulic jumps that occur near the bottom and short-circuit the downscale energy transfer. This prolem is not independent of the undersampling issued discussed in Section 6.1.

Figure 13. Dissipation rates averaged on the neutral density surfaces. The vertical axis is depth plotted both in density (left) and approximate depth (right). The dissipation rate averaged along isopycnals are shown in the horizontal axis. The red and black crosses show estimates by Huussen et al. (2012) (red indicates the arithmetic mean and 95% confidence interval of the observed dissipation rate, and black indicates the mean and confidence interval estimated by fitting to a log-normal distribution). The dissipation rate necessary to explain the meridional overturning circulation across 32°S is shown by diamonds with ±2 standard errors; **mcd** (Macdonald, 1998), **gan** (Ganachaud & Wunsch, 2000), **bry** (Bryden & Beal, 2001), and **slo** (Sloyan & Rintoul, 2001) used inverse calculations based on hydrographic observations and **fer** (Ferron & Marotzke, 2003) was output of a data-assimilated general circulation model. ϵ_0 with the vertical gray dotted lines is the standard dissipation rate of the Garrett-Munk internal wave model. In (a), our estimates are shown by black rectangles where the right and left edges show the 95% confidence interval and the vertical segment is the median. In (b), our estimates by three different methods are shown by cyan, red, and black rectangles. The cyan rectangles show the 95% confidence interval with central segment showing the median for estimates with assumed unobserved mixing events which is about 10 times stronger than the mean in each bin of f in Equation 17. The red rectangles show the same quantity with assumed bottom effects (see text for detail). The black rectangles show the same quantity with both the assumed unobserved mixing events and bottom effects. Adapted from Figure 9 of Huussen et al. (2012).

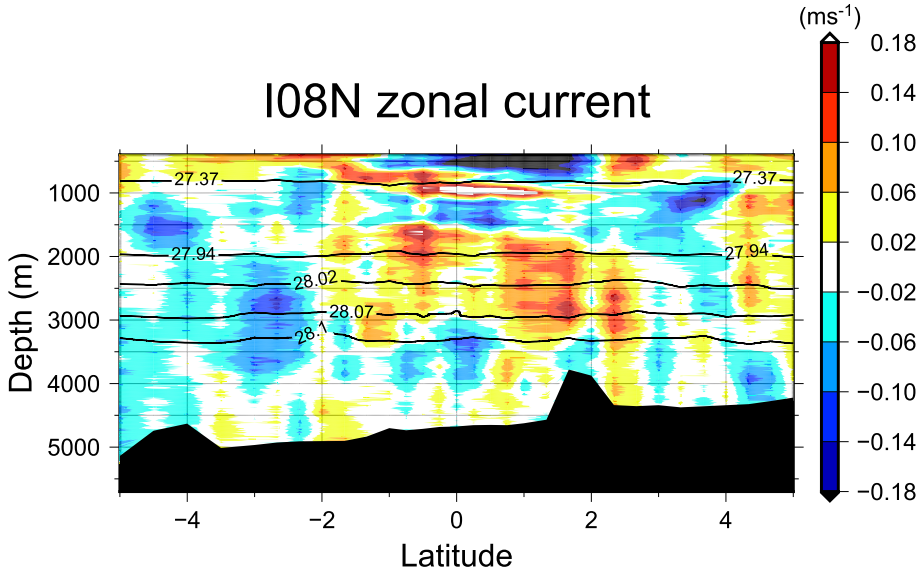

Figure 14. Zonal current measured along 80°E by a LADCP during the 2019 cruise (40NZ20191205, Table A1). Positive is eastward. Black contours show the neutral densities.

To test for near-bottom effects, we compare Figure 8 with the near-bottom mixing observed by microstructure measurements shown in Figure 4 of Decloedt and Luther (2010). Their "Observed" curve is close to our "$D_0 = -3.70$" in Figure 8 for $z > 500$ where z is the height above bottom. The "Observed" curve deviates from "$D_0 = -3.70$" at $z < 500$m and reaches a value between 10^{-3} and $10^{-2.9}$ m^{2}s^{-1}. This value is close to the estimated diapycnal diffusivity of (13–15) $\times 10^{-4}$m^{2}s^{-1} across $\gamma^n = 28.2$ (confined < 700 m from the seabed) in the Perth Basin using heat budget measured by a set of year-long mooring observation (Sloyan, 2006). We include an imaginary bottom dissipation by adding a linearly increasing bottom dissipation, indicated by the dotted lines on Figure 8. We repeat the spatial integration with this profile. The result (Figure 13b, red rectangles) shows an almost twofold increase of turbulence for near bottom density layers $\gamma^n > 28.02$.

When both undersampling and unparameterized bottom effects are included (Figure 13b, black rectangles), our parameterized mixing comes within the uncertainty of the mixing required by the meridional overturning circulation, in particular for deep layers ($\gamma^n > 28$). The reason for the shortage of mixing in the middle to upper layers ($27.83 > \gamma^n$) is not clear. One possibility is discussed in Section 6.3.

6.3. Equator

Using a set of ADCP moorings deployed for more than a year at different latitudes in North Western Pacific along 143°E, Zhang et al. (2018) have shown that the parameterization Equation 1 fails to capture the elevated mixing estimated by the Richardson-number based method. In the equatorial region, the mixing is supported by sub-inertial shear instability of zonal currents. In the Indian ocean, an equatorial cross section along 80°E of zonal currents also shows a number of zonal jets (Figure 14). The change in sign of the jets with vertical scales of 100–1,000 m results in vertical shear likely fueling instability.

The jet structure extends to a depth of almost 4,000 m and covers density surfaces above $\gamma^n = 28.1$.

Other possible mechanisms in the equatorial oceans have been proposed. Holmes et al. (2016), for example, have proposed a mechanism based on the observation of intensified (>10^{-3}m^{2}s^{-1}) mixing over the bottom 700 m in the equatorial Pacific, where equatorial waves near the surface drive near-bottom mixing through the horizontal component of the Earth's rotation (Delorme & Thomas, 2019) and/or inertial instability. This mechanism works over smooth topography. Tanaka et al. (2015) have discussed tropical instability waves near the surface can radiate internal waves downward. Muench and Kunze (1999) have pointed out a possible dissipation mechanism wherein equatorial deep jets act as critical layers for background internal waves. Our data cannot resolve these mechanisms but are not inconsistent in showing downward near-inertial energy propagation near equator (about 4°N, Figure 3).

7. Conclusions

Using CTD and LADCP data collected along sections on cruises upto 2020, we investigated diapycnal mixing in the Indian Ocean, which varies both temporally and spatially. On a meridional section nominally along 95°E, the spatial variation was larger than the temporal variation. The spatial distribution or geography of mixing reveals a contrast between the rough and relatively shallow western basins which are more turbulent than the eastern basins. We also developed a model of depth-dependent dissipation in the Indian Ocean as a function of bottom roughness and wind input. The output of the model is available in Supporting Information (ParamDiffusivity.dat). The mixing integrated north of 35°S latitude is insufficient to explain the meridional overturning circulation in the Indian Ocean. We argue that unobserved mixing events, possibly on continental shelves and slopes, and unparameterized physics including near-bottom and equatorial processes are candidates for the shortage of mixing.

The implications of the present analysis are constrained by the parameterization Equation 1 and the paucity of data. Direct measurements of turbulence by autonomous platform are becoming feasible (Roemmich et al., 2019) and show promise to overcome these constraints, but measurements near the bottom and on continental shelves will remain difficult. A combined approach with traditional ship-based and mooring observations (e.g., McPhaden et al., 2009) is required to close the buoyancy budget in the meridional overturning circulation.

Appendix A: Hydrographic Data

The cruises are listed in Table A1.

Table A1
Hydrographic Data

Section[a]	Year	
I08°S–I09°N	1995	316N145_5
		316N145_6
	2007	33RR20070204
		33RR20070322
	2016	33RR20160208
		33RR20160321
I05	1995	316N145_7
		316N145_9
	2002	74AB20020301
I03–I04	1995	316N145_8
		316N145_9
	2003	49NZ20031209
I08 N	1995	316N145_7
	2019	49NZ20191205
I10	1995	316N145_13
	2015	49NZ20151223
I07	1995	316N145_9
		316N145_10
	2018	33RO20180423
		49NZ20191229
I06S	2008	33RR20080204
	2019	325020190403

Table A1
Continued

Section[a]	Year	
I01	1995	316N145_11
		316N145_12
I02	1995	316N145_14
		316N145_15
IR	1995	3175MB95_02
		3175MB95_04
		3175MB95_07

[a]World Ocean Circulation Experiment Hydrography Program section designation

The LADCP data from 2009 occupation of the I05 section (33RR20090320) are systematically weaker (the median of all shear spectra for 2009 is uniformly lower than that for 2002 and 1995 by a factor of 0.3–0.8 at all wavelengths) and were not used.

Appendix B: Slab Model

Surface winds excite internal waves at local inertial frequency, and this effect is quantified through use of the slab model (Pollard & Millard Jr, 1970). In the slab model, the damping coefficient $r = 0.15 \times f$ where f is the local Coriolis frequency. Mixed layer depth is fixed at 50 m. The slab model is driven by MERRA-2 wind stress (Modeling & Office, 2015) at an hourly interval. The wind speed at 10 m height is converted to the surface stress using the bulk formula (Large & Pond, 1981). For input of the parameterization (Equation 17), the output of the slab model is averaged over time. Expecting that interannual variability is smaller compared to seasonal variability, we averaged only those years when ship observation (Table A1) took place, i.e., years 1994, 1995, 2001, 2003, 2004, 2006, 2007, 2015, 2016, 2018, an 2019. Figure 9 shows the averaged wind power input.

Appendix C: Statistics of Dissipation Rate

Homogeneous turbulence produces dissipation that follows a lognormal distribution Yamazaki (1990). The theory applies at length scales smaller than the forcing at the low wavenumber end of the spectrum and larger than the Kolmogorov scale, which are orders of millimeters to centimeters in the ocean (Yamazaki et al., 1990). Gregg et al. (1993) have observed that dissipation averaged in a vertical 10-m long bin also follows a lognormal distribution and have hypothesized that this is due to the generation of turbulence by a highly skewed shear moment of forth order $\langle S^4 \rangle$, which is incorporated in the parameterization (Equations 1 and 3). If this hypothesis is correct, the most *efficient* way to estimate an average over long time scale of dissipation rate is the maximum likelihood estimator proposed by Baker and Gibson (1987)

$$\hat{X}_{\text{mle}} = \exp\left(\hat{\mu} + \frac{\hat{\sigma}^2}{2}\right), \tag{C1}$$

where

$$\hat{\mu} = \frac{1}{n}\sum^{n} \ln X \tag{C2}$$

$$\hat{\sigma}^2 = \frac{1}{n-1}\sum^{n} (\ln X - \mu)^2 \tag{C3}$$

rather than a simple arithmetic mean

$$\hat{X}_{\text{am}} = \frac{1}{n}\sum^{n} X. \tag{C4}$$

Davis (1996) has suggested use of an arithmetic mean (C4) over (C1) for observed data because of the danger of assuming a parametric distribution, the possibility that measurements made only in a single direction with implicit averaging might invalidate the lognormal assumptions, and the presence of noise in the data.

In Figure 6, at most 3 data are used for averaging. With this paucity of data, the efficiency of the maximum likelihood estimator (C1) could be advantageous, despite the problems pointed out by Davis (1996). Figure C1 compares the probability distribution function of (C4) and (C1) for three samples drawn from a lognormal distribution. We used Equation 14 modified for three samples and integrated numerically as well as Equation 22 in Davis (1996) to calculate the probability density functions for the arithmetic mean and maximum likelihood estimator, respectively. Although the much smaller spread of the maximum likelihood estimator made it more efficient, it suffers from a larger bias than the arithmetic mean. The tendency of the maximum likelihood estimator to underestimate at the cost of efficiency is found for other combinations of μ and σ. Because of this bias, in addition to the danger of assuming a lognormal distribution, we use the arithmetic mean in Section 3.4, Figures 4ab, and 6.

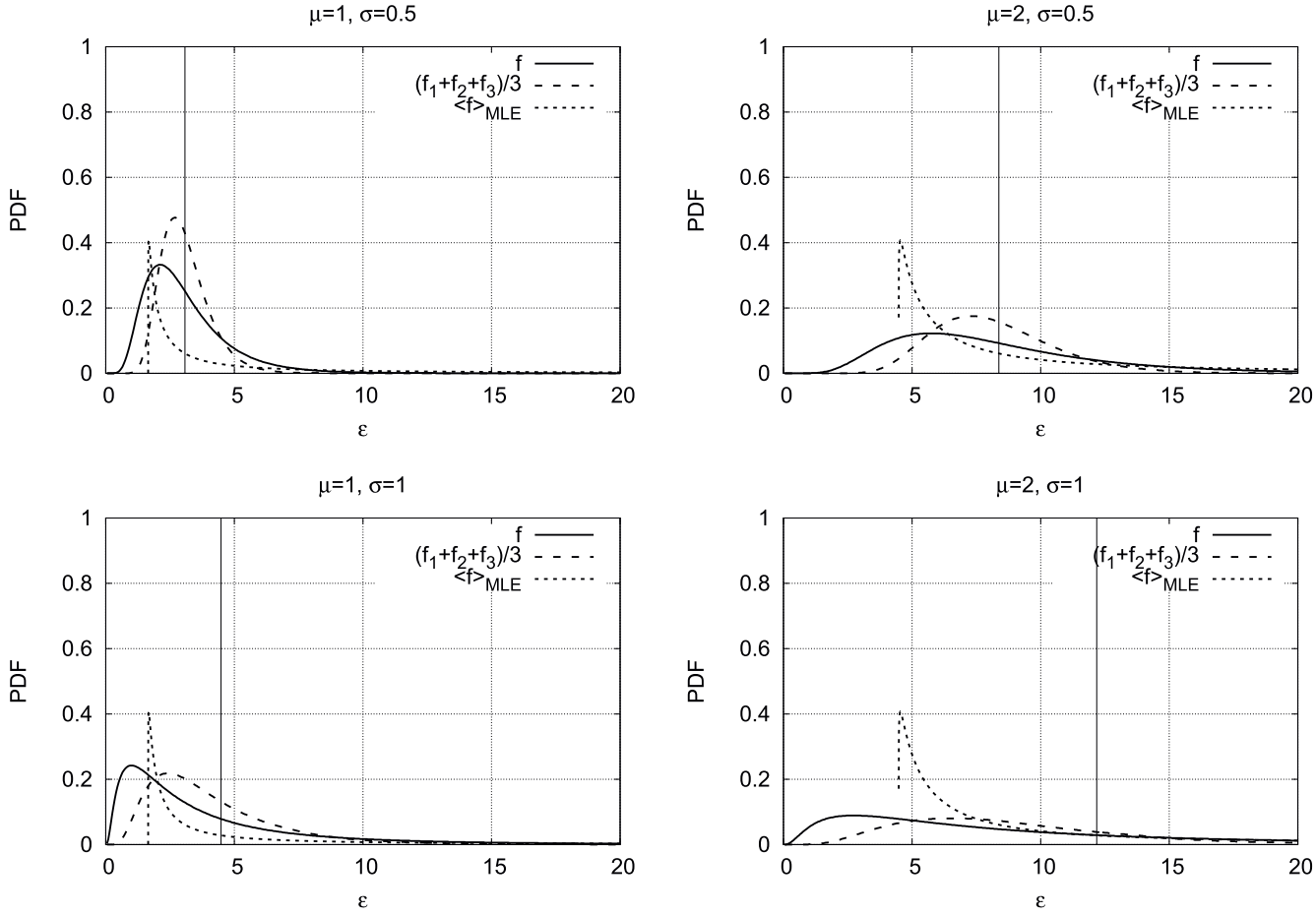

Figure C1. Probability density function of dissipation ϵ estimated by (dashed line) arithmetic mean (C4) and by (dotted line) maximum likelihood estimator (C1) for a sample size of three drawn from log normal distributions of various μ and σ values (mean and standard deviation in the logarithmic space) shown on the title of each panel. The true distribution is shown by solid line with its average by vertical solid line.

Data Availability Statement

All CTD data are available from CCHDO (https://cchdo.ucsd.edu). LADCP data on US ships are available from National Centers for Environmental Information (https://www.ncei.noaa.gov). The project started before these archived data were open to the public and some LADCP data had been provided by Drs. Chereskin (Scripps Institution of Oceanography) and Kosro (Oregon State University). LADCP data on Japanese ships are available from JAMSTEC (http://www.godac.jamstec.go.jp/darwin/e). The code for the analysis is available from the first author's GitHub repository (https://github.com/kkats/physical-oceanography/tree/master/observation). Dr. Kouketsu helped us in preliminary processing of LADCP data for I03 and I04. The project started during KK's visit to SIO.

Acknowledgments
All CTD data are available from CCHDO (https://cchdo.ucsd.edu). LADCP data on US ships are available from National Centers for Environmental Information (https://www.ncei.noaa.gov). The project started before these archived data were open to the public and some LADCP data had been provided by Drs. Chereskin (Scripps Institution of Oceanography) and Kosro (Oregon State University). LADCP data on Japanese ships are available from JAMSTEC (http://www.godac.jamstec.go.jp/darwin/e). The code for the analysis is available from the first author's GitHub repository (https://github.com/kkats/physical-oceanography/tree/master/observation). Dr. Kouketsu helped us in preliminary processing of LADCP data for I03 and I04. The project started during KK's visit to SIO.

References

Alford, M. H., Cronin, M. F., & Klymak, J. M. (2012). Annual cycle and depth penetration of wind-generated near-inertial internal waves at ocean station papa in the northeast pacific. *Journal of Physical Oceanography*, *42*(6), 889–909. https://doi.org/10.1175/jpo-d-11-092.1

Alford, M. H., & Whitmont, M. (2007). Seasonal and spatial variability of near-inertial kinetic energy from historical moored velocity records. *Journal of Physical Oceanography*, *37*(8), 2022–2037. https://doi.org/10.1175/jpo3106.1

Arbic, B. K., Wallcraft, A. J., & Metzger, E. J. (2010). Concurrent simulation of the eddying general circulation and tides in a global ocean model. *Ocean Modelling*, *32*(3–4), 175–187. https://doi.org/10.1016/j.ocemod.2010.01.007

Baker, M. A., & Gibson, C. H. (1987). Sampling turbulence in the stratified ocean: Statistical consequences of strong intermittency. *Journal of Physical Oceanography*, *17*(10), 1817–1836. https://doi.org/10.1175/1520-0485(1987)017<1817:stitso>2.0.co;2

Becker, J. J., Sandwell, D. T., Smith, W. H. F., Braud, J., Binder, B., Depner, J., et al. (2009). Global bathymetry and elevation data at 30 arc seconds resolution: SRTM30_PLUS. *Marine Geodesy*, *32*, 355–371. https://doi.org/10.1080/01490410903297766

Bracco, A., LaCasce, J. H., & Provenzale, A. (2000). Velocity probability density functions for oceanic floats. *Journal of Physical Oceanography*, *30*(3), 461–474. https://doi.org/10.1175/1520-0485(2000)030<0461:vpdffo>2.0.co;2

Bryden, H. L., & Beal, L. M. (2001). Role of the agulhas current in Indian Ocean circulation and associated heat and freshwater fluxes. *Deep Sea Research Part I*, *48*(8), 1821–1845. https://doi.org/10.1016/s0967-0637(00)00111-4

Chinn, B. S., Girton, J. B., & Alford, M. H. (2016). The impact of observed variations in the shear-to-strain ratio of internal waves on inferred turbulent diffusivities. *Journal of Physical Oceanography*, *46*(11), 3299–3320. https://doi.org/10.1175/jpo-d-15-0161.1

D'Asaro, E. A., & Perkins, H. (1984). A near-inertial internal wave spectrum for the Sargasso Sea in late summer. *Journal of Physical Oceanography*, *14*(3), 489–505. https://doi.org/10.1175/1520-0485(1984)014<0489:ANIIWS>2.0.CO;2

Davis, R. E. (1996). Sampling turbulent dissipation. *Journal of Physical Oceanography*, *26*(3), 341–358. https://doi.org/10.1175/1520-0485(1996)026<0341:STD>2.0.CO;2

Decloedt, T., & Luther, D. S. (2010). On a simple empirical parameterization of topography-catalyzed diapycnal mixing in the abyssal ocean. *Journal of Physical Oceanography*, *40*(3), 487–508. https://doi.org/10.1175/2009jpo4275.1

Delorme, B. L., & Thomas, L. N. (2019). Abyssal mixing through critical reflection of equatorially trapped waves off smooth topography. *Journal of Physical Oceanography*, *49*(2), 519–542. https://doi.org/10.1175/JPO-D-18-0197

Drijfhout, S. S., & Naveira Garabato, A. C. (2008). The zonal dimension of the Indian Ocean meridional overturning circulation. *Journal of Physical Oceanography*, *38*(2), 359–379. https://doi.org/10.1175/2007JPO3640.1

Ferron, B., & Marotzke, J. (2003). Impact of 4D-variational assimilation of WOCE hydrography on the meridional circulation of the Indian Ocean. *Deep-Sea Research Part II*, *50*, 2005–2021. https://doi.org/10.1016/S0967-0645(03)00043-2

Ganachaud, A., & Wunsch, C. (2000). Improved estimates of global ocean circulation, heat transport and mixing from hydrographic data. *Nature*, *408*(6811), 453–457. https://doi.org/10.1038/35044048

Gargett, A. E. (2003). Differential diffusion: An oceanographic primer. *Progress in Oceanography*, *56*(3–4), 559–570. https://doi.org/10.1016/s0079-6611(03)00025-9

Garrett, C. (2001). What is the "near-inertial" band and why is it different from the rest of the internal wave spectrum? *Journal of Physical Oceanography*, *31*(4), 962–971. https://doi.org/10.1175/1520-0485(2001)031<0962:witnib>2.0.co;2

Gill, A. E. (1984). On the behavior of internal waves in the wakes of storms. *Journal of Physical Oceanography*, *14*(7), 1129–1151. https://doi.org/10.1175/1520-0485(1984)014<1129:otboiw>2.0.co;2

Goff, J. A., & Arbic, B. A. (2010). Global prediction of abyssal hill roughness statistics for use in ocean models from digital maps of paleo-spreading rate, paleo-ridge orientation, and sediment thickness. *Ocean Modelling*, *32*(1), 36–43. https://doi.org/10.1016/j.ocemod.2009.10.001

Gouretski, V., & Koltermann, K. P. (2004). *Woce Global Hydrographic Climatology* (Vol. 35). Retrieved from https://www.bsh.de/DE/PUBLIKATIONEN/Anlagen/Downloads/Meer_und_Umwelt/Berichte-des-BSH/Berichte-des-BSH_35.html

Gregg, M. C., Seim, H. E., & Percival, D. B. (1993). Statistics of shear and turbulent dissipation profiles in random internal wave fields. *Journal of Physical Oceanography*, *23*(8), 1777–1799. https://doi.org/10.1175/1520-0485(1993)023<1777:SOSATD>2.0.CO;2

Henyey, F. S., Wright, J., & Flatté, S. M. (1986). Energy and action flow through the internal wave field: An eikonal approach. *Journal of Geophysical Research*, *91*(C7), 8487–8495. https://doi.org/10.1029/jc091ic07p08487

Hernández-Guerra, A., & Talley, L. D. (2016). Meridional overturning transports at 30s in the Indian and Pacific oceans in 2002–2003 and 2009. *Progress in Oceanography*, *146*, 89–120. https://doi.org/10.1016/j.pocean.2016.06.005

Hibiya, T., & Nagasawa, M. (2004). Latitudinal dependence of diapycnal diffusivity in the thermocline estimated using a finescale parameterization. *Geophysical Research Letters*, *31*(1). https://doi.org/10.1029/2003gl017998

Holmes, R. M., Moum, J. N., & Thomas, L. N. (2016). Evidence for seafloor-intensified mixing by surface-generated equatorial waves. *Geophysical Research Letters*, *43*(3), 1202–1210. https://doi.org/10.1002/2015gl066472

Huussen, T., Naveira-Garabato, A., Bryden, H., & McDonagh, E. (2012). Is the deep indian ocean moc sustained by breaking internal waves? *Journal of Geophysical Research*, *117*(C8). https://doi.org/10.1029/2012jc008236

Ijichi, T., St. Laurent, L., Polzin, K. L., & Toole, J. M. (2020). How variable is mixing efficiency in the abyss? *Geophysical Research Letters*, *47*(7), e2019GL086813. https://doi.org/10.1029/2019GL086813

IOC, S., & IAPSO. (2010) The international thermodynamic equation of seawater – 2010: Calculation and use of thermodynamic properties. *Intergovernmental Oceanographic Commission Manual and Guides*. *56*, 196.
Jackett, D. R., & McDougall, T. J. (1997). A neutral density variable for the world's oceans. *Journal of Physical Oceanography*, *27*(2), 237–263. https://doi.org/10.1175/1520-0485(1997)027<0237:ANDVFT>2.0.CO;2
Jayasankar, T., Murtugudde, R., & Eldho, T. (2019). The Indian Ocean deep meridional overturning circulation in three ocean reanalysis products. *Geophysical Research Letters*, *46*(21), 12146–12155. https://doi.org/10.1029/2019gl084244
Klocker, A., & McDougall, T. J. (2010). Influence of the nonlinear equation of state on global estimates of dianeutral advection and diffusion. *Journal of Physical Oceanography*, *40*(8), 1690–1709. https://doi.org/10.1175/2010JPO4303.110.1175/2010JPO4303.1
Kunze, E. (1985). Near-inertial wave propagation in geostrophic shear. *Journal of Physical Oceanography*, *15*(5), 544–565. https://doi.org/10.1175/1520-0485(1985)015<0544:NIWPIG>2.0.CO;2
Kunze, E. (2017). Internal-wave-driven mixing: Global geography and budgets. *Journal of Physical Oceanography*, *47*(6), 1325–1345. https://doi.org/10.1175/JPO-D-16-0141.1
Kunze, E., Firing, E., Hummon, J. M., Chereskin, T. K., & Thurnherr, A. M. (2006). Global abyssal mixing inferred from lowered adcp shear and ctd strain profiles. *Journal of Physical Oceanography*, *36*(8), 1553–1576. https://doi.org/10.1175/jpo2926.1
Large, W. G., & Pond, S. (1981). Open ocean momentum flux measurements in moderate to strong winds. *Journal of Physical Oceanography*, *11*(3), 324–336. https://doi.org/10.1175/1520-0485(1981)011<0324:oomfmi>2.0.co;2
Macdonald, A. (2016). Cruise report of the 2016 i08s us go-ship reoccupation. *Tech. Rep. No. Release Draft*, *1*. https://doi.org/10.7942/C2H59N
Macdonald, A. M. (1998). The global ocean circulation: A hydrographic estimate and regional analysis. *Progress in Oceanography*, *41*(3), 281–382. https://doi.org/10.1016/s0079-6611(98)00020-2
MacKinnon, J. A., & Winters, K. B. (2005). Subtropical catastrophe: Significant loss of low-mode tidal energy at 28.9. *Geophysical Research Letters*, *32*(15). https://doi.org/10.1029/2005gl023376
Marshall, J., & Speer, K. (2012). Closure of the meridional overturning circulation through southern ocean upwelling. *Nature Geoscience*, *5*(3), 171–180. https://doi.org/10.1038/ngeo1391
McComas, C. H., & Müller, P. (1981). Time scales of resonant interactions among oceanic internal waves. *Journal of Physical Oceanography*, *11*(2), 139–147. https://doi.org/10.1175/1520-0485(1981)011<0139:tsoria>2.0.co;2
McPhaden, M. J., Meyers, G., Ando, K., Masumoto, Y., Murty, V. S. N., Ravichandran, M., et al. (2009). RAMA: The research moored array for African–Asian–Australian monsoon analysis and prediction. *Bulletin of the American Meteorological Society*, *90*(4), 459–480. https://doi.org/10.1175/2008BAMS2608.1
Modeling, G., & Office, A. (2015).MERRA-2 tavg1_2d_slv_Nx: 2d,1-hourly,time-averaged,single-level,assimilation,single-level diagnostics V5.12.4 (M2T1NXSLV), *The second Modern-Era Retrospective analysis for Research and Applications*. https://doi.org/10.5067/VJAFPLI1CSIV
Muench, J. E., & Kunze, E. (1999). Internal wave interactions with equatorial deep jets. Part I: Momentum-flux divergences. *Journal of Physical Oceanography*, *29*(7), 1453–1467. https://doi.org/10.1175/1520-0485(1999)029<1453:IWIWED>2.0.CO;2
Munk, W., & Wunsch, C. (1998). Abyssal recipes II: Energetics of tidal and wind mixing. *Deep-Sea Research Part I*, *45*(12), 1977–2010. https://doi.org/10.1016/S0967-0637(98)00070-3
Orsi, A. H., Whitworth, T., III, & Nowlin, W. D., Jr (1995). On the meridional extent and fronts of the antarctic circumpolar current. *Deep Sea Research Part I*, *42*(5), 641–673. https://doi.org/10.1016/0967-0637(95)00021-w
Pollard, R. T., & Millard, R. C., Jr (1970). Comparison between observed and simulated wind-generated inertial oscillations. *Deep-Sea Research*, *17*(4), 813–821. https://doi.org/10.1016/0011-7471(70)90043-4
Polzin, K., Kunze, E., Hummon, J., & Firing, E. (2002). The finescale response of lowered adcp velocity profiles. *Journal of Atmospheric and Oceanic Technology*, *19*(2), 205–224. https://doi.org/10.1175/1520-0426(2002)019<0205:tfrola>2.0.co;2
Polzin, K. L., & Lvov, Y. V. (2011). Toward regional characterizations of the oceanic internal wavefield. *Reviews of Geophysics*, *49*(4). https://doi.org/10.1029/2010rg000329
Polzin, K. L., Naveira Garabato, A. C., Huussen, T. N., Sloyan, B. M., & Waterman, S. (2014). Finescale parameterizations of turbulent dissipation. *Journal of Geophysical Research: Oceans*, *119*(2), 1383–1419. https://doi.org/10.1002/2013jc008979
Polzin, K. L., Toole, J. M., & Schmitt, R. W. (1995). Finescale parameterizations of turbulent dissipation. *Journal of Physical Oceanography*, *25*(3), 306–328. https://doi.org/10.1175/1520-0485(1995)025<0306:fpotd>2.0.co;2
Purkey, S. G., & Johnson, G. C. (2010). Warming of global abyssal and deep southern ocean waters between the 1990s and 2000s: Contributions to global heat and sea level rise budgets. *Journal of Climate*, *23*(23), 6336–6351. https://doi.org/10.1175/2010jcli3682.1
Robbins, P. E., & Toole, J. M. (1997). The dissolved silica budget as a constraint on the meridional overturning circulation of the Indian Ocean. *Deep Sea Research Part I*, *44*(5), 879–906. https://doi.org/10.1016/s0967-0637(96)00126-4
Roemmich, D., Alford, M. H., Claustre, H., Johnson, K., King, B., Moum, J., et al. (2019). On the future of argo: A global, full-depth, multi-disciplinary array. *Frontiers in Marine Science*, *6*, 439. https://doi.org/10.3389/fmars.2019.00439
Ruddick, B. (1983). A practical indicator of the stability of the water column to double-diffusive activity. *Deep-Sea Research Part A*, *30*(10), 1105–1107. https://doi.org/10.1016/0198-0149(83)90063-8
Sloyan, B. M. (2006). Antarctic bottom and lower circumpolar deep water circulation in the eastern Indian Ocean. *Journal of Geophysical Research*, *111*(C2). https://doi.org/10.1029/2005jc003011
Sloyan, B. M., & Rintoul, S. R. (2001). The southern ocean limb of the global deep overturning circulation. *Journal of Physical Oceanography*, *31*(1), 143–173. https://doi.org/10.1175/1520-0485(2001)031<0143:tsolot>2.0.co;2
Talley, L. D. (2013). Closure of the global overturning circulation through the Indian, Pacific, and southern oceans: Schematics and transports. *Oceanography*, *26*(1), 80–97. https://doi.org/10.5670/oceanog.2013.07
Tanaka, Y., Hibiya, T., & Sasaki, H. (2015). Downward lee wave radiation from tropical instability waves in the central equatorial Pacific Ocean: A possible energy pathway to turbulent mixing. *Journal of Geophysical Research: Oceans*, *120*(11), 7137–7149. https://doi.org/10.1002/2015JC011017
Thurnherr, A. M. (2012). The finescale response of lowered adcp velocity measurements processed with different methods. *Journal of Atmospheric and Oceanic Technology*, *29*(4), 597–600. https://doi.org/10.1175/jtech-d-11-00158.1
Toggweiler, J., & Samuels, B. (1998). On the ocean's large-scale circulation near the limit of no vertical mixing. *Journal of Physical Oceanography*, *28*(9), 1832–1852. https://doi.org/10.1175/1520-0485(1998)028<1832:otosls>2.0.co;2
Visbeck, M. (2002). Deep velocity profiling using lowered acoustic doppler current profilers: Bottom track and inverse solutions. *Journal of Atmospheric and Oceanic Technology*, *19*(5), 794–807. https://doi.org/10.1175/1520-0426(2002)019<0794:dvpula>2.0.co;2

Waterhouse, A. F., Kelly, S. M., Zhao, Z., MacKinnon, J. A., Nash, J. D., Simmons, H., et al. (2018). Observations of the Tasman Sea internal tide beam. *Journal of Physical Oceanography*, *48*(6), 1283–1297. https://doi.org/10.1175/JPO-D-17-0116.1

Waterhouse, A. F., MacKinnon, J. A., Nash, J. D., Alford, M. H., Kunze, E., Simmons, H. L., et al. (2014). Global patterns of diapycnal mixing from measurements of the turbulent dissipation rate. *Journal of Physical Oceanography*, *44*(7), 1854–1872. https://doi.org/10.1175/jpo-d-13-0104.1

Webb, D. J., & Suginohara, N. (2001). Vertical mixing in the ocean. *Nature*, *409*(6816), 37. https://doi.org/10.1038/35051171

Whalen, C. B. (2021). Best practices for comparing ocean turbulence measurements across spatiotemporal scales. *Journal of Atmospheric and Oceanic Technology*, *38*(4), 837–841. https://doi.org/10.1175/JTECH-D-20-0175.1

Whalen, C. B., MacKinnon, J. A., & Talley, L. D. (2018). Large-scale impacts of the mesoscale environment on mixing from wind-driven internal waves. *Nature Geoscience*, *11*(11), 842–847. https://doi.org/10.1038/s41561-018-0213-6

Yamazaki, H. (1990). Breakage models: Lognormality and intermittency. *Journal of Fluid Mechanics*, *219*, 181–193. https://doi.org/10.1017/s0022112090002907

Yamazaki, H., & Lueck, R. (1990). Why oceanic dissipation rates are not lognormal. *Journal of Physical Oceanography*, *20*(12), 1907–1918. https://doi.org/10.1175/1520-0485(1990)020<1907:wodran>2.0.co;2

Yamazaki, H., Lueck, R. G., & Osborn, T. (1990). A comparison of turbulence data from a submarine and a vertical profiler. *Journal of Physical Oceanography*, *20*(11), 1778–1786. https://doi.org/10.1175/1520-0485(1990)020<1778:ACOTDF>2.0.CO;2

You, Y. (1999). Dianeutral mixing, transformation and transport of the deep water of the Indian Ocean. *Deep-Sea Research Part I*, *46*(1), 109–148. https://doi.org/10.1016/S0967-0637(98)00058-2

Zhang, Z., Qiu, B., Tian, J., Zhao, W., & Huang, X. (2018). Latitude-dependent finescale turbulent shear generations in the pacific tropical-extratropical upper ocean. *Nature Communications*, *9*(1), 1–13. https://doi.org/10.1038/s41467-018-06260-8